The Astrophysical Journal, 991:76 (31pp), 2025 September 20 https://doi.org/10.3847/1538-4357/ade440

Star Clusters in the Near-ultraviolet-optical-near-infrared: Spectral Energy Distribution Modeling with Direct Markers of Gas and Dust Emission

Kiana F. Henny[1], Daniel A. Dale[1], Rupali Chandar[2], Médéric Boquien[3], David A. Thilker[4], Bradley C. Whitmore[5], Janice C. Lee[5], M. Jimena Rodriguez[5,6], Daniel Maschmann[5], Aida Wofford[7,8], Rémy Indebetouw[9], Leonardo Úbeda[5], Brent Groves[10], Hamid Hassani[11], Kirsten L. Larson[12], Thomas G. Williams[13], Kathryn Grasha[14,15], Francesca Pinna[16,17], and Stephen Hannon[18]

[1] Department of Physics and Astronomy, University of Wyoming, Laramie, WY 82071, USA; khenny@uwyo.edu
[2] Ritter Astrophysical Research Center, University of Toledo, Toledo, OH 43606, USA
[3] Université Côte d'Azur, Observatoire de la Côte d'Azur, CNRS, Laboratoire Lagrange, 06000, Nice, France
[4] Department of Physics and Astronomy, The Johns Hopkins University, Baltimore, MD 21218, USA
[5] Space Telescope Science Institute, 3700 San Martin Drive, Baltimore, MD 21218, USA
[6] Instituto de Astrofísica de La Plata, CONICET–UNLP, Paseo del Bosque S/N, B1900FWA La Plata, Argentina
[7] Instituto de Astronomía, Universidad Nacional Autónoma de México, Unidad Académica en Ensenada, Km 103 Carr. Tijuana-Ensenada, Ensenada, B.C., C.P. 22860, México
[8] Department of Astronomy and Astrophysics, University of California, San Diego, 9500 Gilman Drive, La Jolla, CA 92093, USA
[9] National Radio Astronomy Observatory, 520 Edgemont Road, Charlottesville, VA 22903, USA; Department of Astronomy, University of Virginia, Charlottesville, VA 22904, USA
[10] International Centre for Radio Astronomy Research, University of Western Australia, 7 Fairway, Crawley, 6009 WA, Australia
[11] Department of Physics, University of Alberta, Edmonton, AB T6G 2E1, Canada
[12] AURA for the European Space Agency (ESA), Space Telescope Science Institute, 3700 San Martin Drive, Baltimore, MD 21218, USA
[13] Sub-department of Astrophysics, Department of Physics, University of Oxford, Keble Road, Oxford OX1 3RH, UK
[14] Research School of Astronomy and Astrophysics, Australian National University, Canberra, ACT 2611, Australia
[15] ARC Centre of Excellence for All Sky Astrophysics in 3 Dimensions (ASTRO 3D), Australia
[16] Instituto de Astrofísica de Canarias, C/ Vía Láctea s/n, E-38205, La Laguna, Spain
[17] Departamento de Astrofísica, Universidad de La Laguna, Av. del Astrofísico Francisco Sánchez s/n, E-38206, La Laguna, Spain
[18] Max Planck Institut für Astronomie, Königstuhl 17, 69117 Heidelberg, Germany
Received 2024 October 8; revised 2025 June 9; accepted 2025 June 11; published 2025 September 16

Abstract

The large number of star clusters in nearby galaxies permits us to statistically test the predictions of stellar, dust, and gas models. Using Hubble Space Telescope (HST) broadband plus Hα imaging combined with JWST near-infrared imaging, we use a total of 10 filters spanning near-ultraviolet through near-infrared wavelengths to model key physical parameters, including age, mass, and reddening, of 6130 star clusters in 16 nearby spiral galaxies from the Physics at High Angular resolution in Nearby GalaxieS sample, focusing on their ages, masses, and reddenings. We find that HST/Hα and JWST/NIRCam 2–3.6 μm photometry significantly improves our ability to disentangle the age–reddening degeneracy between young, gas- and dust-rich clusters and older, dustless clusters. The near-infrared data provide strong constraints on hot continuum dust and small polycyclic aromatic hydrocarbon emission for populations where gas and dust are present. These hot dust constraints demonstrate that Bruzual & Charlot stellar population models do not align with the observed near-ultraviolet-optical-near-infrared spectral energy distributions of star clusters in the first 10 Myr. We note that for old and low-metallicity globular clusters, the inclusion of narrowband Hα and/or broadband near-infrared data does not improve the determination of age and reddening parameters, due to the lack of stars capable of heating dust in the near-infrared regime.

Unified Astronomy Thesaurus concepts: Star clusters (1567); Spiral galaxies (1560); Spectral energy distribution (2129); Star forming regions (1565)

1. Introduction

Star clusters are key to understanding the evolution of galaxies over time. Young clusters are the main source of high-energy photons capable of exciting gas and dust in the interstellar medium (ISM), and older clusters provide snapshots of a galaxy's past. In the Local Group, isochrone fitting is a standard approach (LMC/SMC: P. Goudfrooij et al. 2011; D. R. Weisz et al. 2013; P. K. Nayak et al. 2018; W. Narloch et al. 2022; spiral galaxies: L. C. Johnson et al. 2012; H. Kim et al. 2012; B. F. Williams et al. 2012; E. Sabbi et al. 2018; E. Sacchi et al. 2019). Unfortunately, methods to determine key parameters (age, mass, and metallicity) of star clusters in our Local Group, such as isochrone fitting, require us to resolve individual stars in a given cluster, which is only possible in galaxies less than a few hundred kiloparsecs away (Z. Fan et al. 2018). In order to probe a range of galaxy environments and to robustly test theoretical predictions, we need to observe galaxies outside of our Local Group. This means that we must determine how to most accurately model clusters based only on their integrated light, rather than their resolved stellar populations.

Acquiring high-spatial-resolution spectra of a statistically large sample of star clusters is time intensive, and as a result, using imaging combined with spectral energy distribution (SED) modeling is the most efficient way to determine their physical parameters without full spectra. Accurate modeling of

the physical qualities of star clusters is necessary to gain insight into the formation and disruption processes for clusters, the relationship between star and cluster formation, the evolution of cluster mass functions, and more.

However, SED fitting of unresolved star clusters is rife with degeneracies. Due primarily to the past dearth of instruments capable of subarcsecond imaging in the 1–5 μm range, star cluster SED modeling is usually performed in the near-ultraviolet-optical range. Additionally, a previous lack of instruments capable of making observations of dust emission at the same angular resolution as these near-ultraviolet-optical observations means that past works, including LEGUS, LVL, and PHANGS–Hubble Space Telescope (HST), have had to attempt to accurately model dust abundance (through absorption) with only near-ultraviolet-optical data (D. Calzetti et al. 2015; K. Grasha et al. 2015; A. Adamo et al. 2017; M. Messa et al. 2018b,. 2018a; D. O. Cook et al. 2019, 2023; B. C. Whitmore et al. 2020; J. A. Turner et al. 2021; S. Deger et al. 2022; S. Deshmukh et al. 2024; T. McQuaid et al. 2024). One of the most problematic degeneracies we face when trying to determine the physical qualities of clusters is a multifaceted interface between age, metallicity, and reddening (B. C. Whitmore et al. 2011; J. A. Turner et al. 2021; S. Hannon et al. 2022): old, low-metallicity, dust-free clusters are difficult to distinguish from young, dust-rich clusters or intermediate-age, moderately dusty clusters using only broadband optical data. Additionally, a less-than-fully sampled initial mass function (IMF) can also contribute to degeneracy, especially for lower-mass clusters ($<10^3\ M_\odot$; G. Ashworth et al. 2017) that are less likely to have formed the highest-mass stars ($>30\ M_\odot$). These clusters will appear to be similar to slightly older clusters that have already lost their highest-mass stars (M. Fouesneau & A. Lançon 2010; A. Wofford et al. 2011; M. Fouesneau et al. 2012; J. E. Andrews et al. 2014; M. R. Krumholz et al. 2015; G. Ashworth et al. 2017; S. Hannon et al. 2019; R. Orozco-Duarte et al. 2022). Simply performing SED fitting with a "maximalist" parameter space, in which as many parameters as possible can vary across their full range, results in "best fits," which, while fitting the observed near-ultraviolet-optical photometry well, lead to large uncertainties across this degenerate space. Manual inspection often reveals the inaccuracies of these fits, but when dealing with a large catalog of clusters, the task of manual verification is prohibitively time consuming. This limitation means that accurate SED modeling of star clusters has two equally crucial requirements: first, accurately classifying clusters as belonging to categories with specific physical characteristics and restricting their priors (e.g., old/globular clusters with subsolar metallicity versus solar-metallicity clusters), and second, modeling these clusters with priors appropriate for their category (J. Bialopetravičius et al. 2019; J. Bialopetravičius & D. Narbutis 2020; W. Wei et al. 2020; G. Pérez et al. 2021; B. C. Whitmore et al. 2021, L. C. Johnson et al. 2022; S. Hannon et al. 2023; J. Tang et al. 2024; D. A. Thilker et al. 2025).

In this paper, we will describe improvements and limitations of modeling ages, reddening, and masses of star clusters in nearby galaxies with the addition of JWST NIRCam and HST-Hα data and updates to our SED modeling framework, which previously relied on only five-band HST near-ultraviolet-optical broadband photometry. We validate the identification method for old/globular clusters developed by D. A. Thilker et al. (2025). We then implement three physically motivated sets of priors that account for dust and nebular emission for young gas-rich clusters, and low metallicity for old/globular clusters, to model our star cluster catalog.

In Section 2 we give an overview of the observations used in SED modeling. In Section 3, we describe past PHANGS-HST near-ultraviolet-optical SED fitting, modeling updates made to incorporate gas and dust emission, and the priors used for three cluster subpopulations with distinct physical qualities. In Section 4 we will present the results of these SED modeling updates, and in Section 5, we will discuss how modeling with direct markers of gas and dust both improves and complicates our understanding of SED fitting across the near-ultraviolet-near-infrared wavelength range.

2. Observations, Catalogs, and Photometry

2.1. Galaxy Sample and Cluster Catalogs

The Physics at High Angular resolution in Nearby GalaxieS (PHANGS) collaboration seeks to understand star formation in spiral galaxies at all scales, from star clusters to spiral arm structure, and how processes across multiple scales interact with and inform each other (A. K. Leroy et al. 2021). The PHANGS data set includes spatially overlapping Atacama Large Millimeter/submillimeter Array (ALMA), MUSE, HST, and JWST observations of nearby spiral galaxies. This multiwavelength data set allows us to study the stars, gas, and dust of this galaxy sample. In this work, we focus on the subset of 16 galaxies compiled in Table 1, which contain 7557 manually identified star clusters observed with HST. These galaxies have all been observed with a single HST pointing except for NGC 628, which has both a "central" and an "eastern" pointing (NGC 628c and NGC 628e, respectively). We use this sample because in addition to broadband imaging in five filters with HST (see details below), all of our target galaxies have narrowband imaging covering the Hα recombination line from HST, and four-filter imaging with NIRCam on JWST; the observations are described later in this section. Because the NIRCam footprint is smaller than the HST footprint, and the HST-Hα data were obtained in a separate program, the intersection of the overlapping maps creates a smaller footprint than the HST broadband footprints alone in some cases, reducing the total number of star clusters with full data coverage from 7557 to 6130 in these 16 galaxies. The galaxies have a range of distances between 9 and 20 Mpc, and are compiled in G. S. Anand et al. (2021), with updates in J. C. Lee et al. (2023). Their distances are listed in Column (2) of Table 1. Their star formation rates were determined by A. K. Leroy et al. (2021) based on total mid-infrared luminosities and have a range between 0.41 $M_\odot \mathrm{yr}^{-1}$ in the case of the dwarf galaxy IC 5332 and as large as 7.6 $M_\odot \mathrm{yr}^{-1}$ for NGC 1672. The stellar masses are determined from Wide-field Infrared Survey Exlporer 1 3.4 μm fluxes, using the prescription in A. K. Leroy et al. (2021).

The PHANGS-HST collaboration has produced catalogs of compact star clusters for each galaxy (J. A. Turner et al. 2021, S. Deger et al. 2022, D. Maschmann et al. 2024a).

Initial source detection was performed primarily with DOLPHOT (A. Dolphin 2016), with a small number of sources added via DAOStarFinder. Sources were detected to the 3.5σ level via simultaneous point-spread function (PSF)-fitting on all filters, with the V band used as the positional reference. From this catalog, for a source to be identified as a

Table 1
Galaxies Observed with HST broadband, HST-Hα, and JWST NIRCam

Galaxy	Distance[a] (Mpc)	4 Pixel Scale (pc)	V-band ap corr	HST Filters
IC 5332	9.01	7.0	−0.59	F275W, F336W, F438W, F555W, F658N (ACS), F814W
NGC 628c	9.84	7.6	−0.75	F275W, F336W, F435W (ACS), F555W, F658N (ACS), F814W (ACS)
NGC 628e	9.84	7.6	−0.72	F275W, F336W, F435W (ACS), F555W, F658N (ACS), F814W (ACS)
NGC 1087	15.85	12.3	−0.67	F275W, F336W, F438W, F555W, F657N, F814W
NGC 1300	18.99	14.7	−0.61	F275W, F336W, F435W (ACS), F555W, F658N (ACS), F814W (ACS)
NGC 1365	19.57	15.2	−0.61	F275W, F336W, F438W, F555W, F657N, F814W
NGC 1385	17.22	13.4	−0.69	F275W, F336W, F438W, F555W, F657N, F814W
NGC 1433	18.94	14.7	−0.62	F275W, F336W, F438W, F555W, F657N, F814W
NGC 1512	17.93	13.9	−0.62	F275W, F336W, F438W, F555W, F658N (ACS), F814W
NGC 1566	17.69	13.7	−0.62	F275W, F336W, F438W, F555W, F658N (ACS), F814W
NGC 1672	19.40	15.0	−0.60	F275W, F336W, F435W (ACS), F555W, F658N (ACS), F814W (ACS)
NGC 3351	9.96	7.7	−0.68	F275W, F336W, F438W, F555W, F657N, F814W
NGC 3627	11.32	8.8	−0.81	F275W, F336W, F438W, F555W, F658N (ACS), F814W
NGC 4254	13.1	10.2	−0.80	F275W, F336W, F438W, F555W, F657N, F814W
NGC 4303	16.99	13.2	−0.74	F275W, F336W, F438W, F555W, F658N (ACS), F814W
NGC 4321	15.21	11.8	−0.69	F275W, F336W, F438W, F555W, F657N, F814W
NGC 7496	18.72	14.5	−0.54	F275W, F336W, F438W, F555W, F657N, F814W

Note.
[a] G. S. Anand et al. 2021.

cluster, it had to have a detection with S/N > 10 in the V band, and a photometric error $\leqslant$0.3 mag in at least two other filters. The faintest sources in the resulting candidate list had V band magnitudes of ∼24.6. Further subsetting was done by computing multiple concentration indices (MCIs) of sources and comparing them to a fiducial extended cluster model, which had a pre-PSF-convolution FWHM of 2 pixels and $\eta = 3$. Fiducial modeled cluster constants were computed for each galaxy. The MCI of a source was determined by averaging the normalized concentration index (NCI) of three sets of radius pairs:

$$\mathrm{MCI} = \overline{\mathrm{NCI}(a, b), \mathrm{NCI}(b, c), \mathrm{NCI}(c, d)} \quad (1)$$

where a, b, c, and d are increasing pixel radii. $\mathrm{MCI_{in}}$ probing the inner portion (a, b, c, d = 1.0, 1.5, 2.0, 2.5) of a source, and $\mathrm{MCI_{out}}$ probing the faint low surface brightness outer portion of sources (a, b, c, d = 2.5, 3.0, 4.0, 5.0) were computed, and sources were selected as cluster candidates if they had $-0.55 \leqslant \mathrm{MCI_{in}} \leqslant 0.45$, and a statistical error of $\mathrm{MCI_{in,err}} \leqslant 0.3$, $\mathrm{MCI_{out,err}} \leqslant 1.0$. All candidates with an absolute V-band magnitude $\geqslant -10$ were kept. Additional restrictions in the MCI plane were implemented to avoid contamination from single-star sources. A full description of the catalog-building method can be found in D. A. Thilker et al. (2022) and J. C. Lee et al. (2022).

Candidate clusters were classified based on source morphology by both a human performing visual inspection and a machine learning algorithm (W. Wei et al. 2020; B. C. Whitmore et al. 2021; S. Hannon et al. 2023). Human-inspected clusters were classified down to a magnitude of ∼24 in the V band, and machine learning identified and classified clusters up to ∼1 mag fainter than that performed by human inspection. Across 38 galaxies, human visual inspection yielded ∼22,000 objects, and machine learning yielded ∼96,000 (including objects also identified via human visual inspection). Clusters were classified into the categories developed by LEGUS and described in A. Adamo et al. (2017) and D. O. Cook et al. (2019): Class 1 clusters have a single peak, are circularly symmetric, and have a radial profile that is extended compared to a point source. Class 2 clusters are similar to Class 1 but have an asymmetric or elongated shape. Class 3 objects are asymmetric with multiple peaks and are deemed stellar associations rather than clusters. Class 4 objects are not compact star clusters or stellar associations. B. C. Whitmore et al. (2021) provided an in-depth description of the visual inspection and morphological classification of candidate clusters in the PHANGS-HST catalog specifically. In this work, we use only the human-classified catalogs of Class 1+2 sources. Human-classified clusters are generally brighter than the machine learning identified and classified clusters, making them a more straightforward sample to work with.

2.2. HST Broadband Data and Photometry

In order to estimate the age, reddening, and mass of each cluster, we fit the SED of each cluster. Previous works have already used HST broadband photometry for this purpose, as summarized below.

The PHANGS-HST data set consists of observations of 38 galaxies in the near-UV (NUV) – U – B – V – I filters (J. C. Lee et al. 2022; PID15454). These 38 galaxies were selected from the PHANGS-ALMA sample of 74 nearby galaxies because they are relatively face-on, avoid the Galactic plane, and have significant molecular cloud populations. Galaxies were observed with WFC3, and archival ACS images were used when available and processed consistently and in conjunction with PHANGS-HST observations. The HST filters used for each galaxy are compiled in Column (4) of Table 1.

Three exposures with subpixel dithering were taken in each of the five filters: F275W (NUV), F336W (U), F435W or F438W (B), F555W (V), and F814W (I). Photometry was performed with a 4 pixel aperture, with the physical size of this aperture for each galaxy listed in Column (3) of Table 1. For a detailed description of how photometry was performed for the PHANGS-HST catalog, see J. C. Lee et al. (2023). Aperture corrections were derived from a sample of bright, relatively isolated star clusters (S. Deger et al. 2022). Aperture

corrections in the *V* band were derived for each galaxy from a sample of isolated, symmetric Class 1+2 clusters, and average values range from −0.54 to −0.81. The specific *V*-band aperture corrections for each galaxy are listed in Table 1. Offsets of −0.19, −0.12, −0.03, and −0.12 mag were then applied to the NUV, *U*, *B*, and *I* band, respectively, for all galaxies.

These HST data were used to conduct the largest star cluster census to date (D. Maschmann et al. 2024a), which yielded a sample of ∼100,000 star clusters and compact associations. Supporting catalogs were released through MAST in 2024 January.

2.3. HST-Hα Observations

We include high angular resolution HST-Hα data to our SEDs, using a combination of archival and new imaging (PI: R. Chandar, GO-17126). Additional HST-Hα data for the PHANGS galaxy sample are being obtained in HST Cycle 31 (PI: D. Thilker, GO-17502). A galaxy either has data in the F658N or F657N filter, depending on its redshift.

The HST-Hα observations are used for two distinct purposes: (1) to assess whether a cluster is very young and gas-rich, and (2) as an additional constraint in SED fitting. To assess if a cluster is likely young and the source of the ionized gas in its immediate vicinity, we use the Hα equivalent width, EW(Hα). We linearly interpolate the cluster stellar continuum flux level $f_{\mathrm{cont},\nu}$ at F658N/F657N from the F555W and F814W bands, then calculate EW(Hα) using this continuum level along with the total narrowband filter flux $f_{\mathrm{total},\nu}$:

$$\mathrm{EW(H}\alpha) = \frac{(f_{\mathrm{total},\nu} - f_{\mathrm{cont},\nu})\Delta\nu c}{f_{\mathrm{cont},\nu}\,\nu_{\mathrm{eff}}^2} \quad (2)$$

where $\Delta\nu = 5.1713\mathrm{e}12$ Hz is the width of the Hα narrowband filter, $f_{\mathrm{total},\nu}$ and $f_{\mathrm{cont},\nu}$ are the total and stellar continuum flux density in janskys, and ν_{eff} is the central frequency of the Hα filter.

As is detailed more in Section 3.2.1, the Hα equivalent width is exclusively used as a flag to identify clusters that are most likely the source of the ionizing photons that are energizing gas within a 4 HST pixel aperture. The EW threshold that we implement was derived empirically, by individually examining every cluster in several galaxies in NUV-optical-near-IR (NIR) filters, and finding an EW value above which the observed Hα emission in star clusters that exhibit Hα above the continuum, is very likely being energized by the cluster in question, given the cluster's SED, color–color location, and gas and dust morphology. Although the neighboring bands we use, F555W and F814W, do both include nebular lines that can account for large fractions of total emission (up to 50%–70% for F555W and up to 25%–50% for F814W) as described in A. E. Reines et al. (2010), calculating the Hα EW without adjusting for the possible presence of these lines will only result in a more conservative identification of star clusters that are likely young and gas-rich. Our empirical and multifaceted determination of the EW threshold mitigates much of the potential bias in the selection of young and gas-rich clusters. Additionally, since we adopt a nebular emission model grid that permits a model to find a best fit of up to 100% of Lyman continuum photons escaping a cluster, we do not anticipate that this conservative approach will result in inappropriate modeled fits.

The Hα flux measured in a 4 HST pixel aperture is subsequently used without continuum subtraction for SED modeling itself. This means we fit the nebular and stellar emission simultaneously, and the multiple nebular lines present in various filters (O III in F555W, N II in F658N, and S III lines in F814W are some of the strongest) will be directly incorporated into modeling without first needing to determine their excess compared to the underlying stellar or nebular continuum.

The extendedness of Hα emission for most young gas-rich clusters means that measurements also can have large nonphotometric uncertainties in multiple ways. If a cluster has a very extended Hα morphology, the measurement in a 4 pixel aperture will not be close to the total Hα emission. In the other direction, in a cluster that is situated in a larger star-forming complex with multiple sources of ionizing photons, it is difficult to say how much of the measured Hα is due to ionization from that cluster, rather than its neighbors. Fortunately, a strong excess of Hα emission relative to neighboring filters heavily influences SED modeling toward models that are compatible with human evaluations of young gas-rich star clusters' physical qualities, regardless of the precise measured flux. We discuss this uncertainty further in Section 3.2.1.

2.4. JWST NIRCam Observations

We also include measurements in four NIRCam filters in our SED fitting. The PHANGS-JWST Treasury program (PI: J. C. Lee, GO-2107; J. C. Lee et al. 2023; T. G. Williams et al. 2024) is a Cycle 1 JWST program that imaged 19 out of 38 PHANGS-HST galaxies, all of which also have integral field unit maps from the Very Large Telescope/MUSE (E. Emsellem et al. 2022). The treasury JWST program imaged these galaxies in four NIRCam filters: F200W, F300M, F335M, and F360M.

Photometry was performed with a 4 pixel aperture (0.″124) in the short wavelength channel in all bands. The background annulus is 2×–3× the aperture size (0.″248–0.″372). The aperture corrections were derived from a sample of isolated, Class 1 clusters (mostly old/globular clusters; OGCs), following the method outlined in S. Deger et al. (2022), with some adjustments. Performing accurate photometry in the NIR with NIRCam is challenging, due to the large number of bright pointlike sources (e.g., red giant stars, asymmetric giant branch stars, young stellar objects, YSOs, etc.) that may be present in both the object aperture and the sky annulus. While some of these might be background objects, others may be part of the cluster itself (i.,e., YSOs). Using the normal method of using the median pixel values and a narrow sky annulus clearly underestimates the sky value, resulting in increasing apparent flux values at all radii out to 20 pixels (0.″62 using the short wavelength NIRCam pixels), even though the cluster is only apparent in the inner few pixels. To address this problem, we determine the sky flux needed to make the mean flux in a 12 pixel radius (0.″37) equal to 98% of the 20 pixel radius value, based on the assumption that there is 2% of the light from a point source from scattered light between these two radii for NIRCam. At a radius of 12 pixels, approximately 98% of the total flux from a cluster is included, based on inspection of the light profiles for bright old globular clusters in our sample. At a radius of 20 pixels, we can be sure that we are including all of the light from a cluster. When the described

correction is performed, the profiles for intermediate-age clusters in the F200W band match those of the brightest old globular clusters and are appropriate for extended clusters. The flux within the 4 pixel object aperture may or may not include one or more background sources, and is intrinsically more uncertain than in the optical wavelengths where there are far fewer background sources. The reader is invited to examine several of the F200W snapshots (e.g., the SED plots in Section 4.1) relative to the HST optical band snapshots to gain a better feeling for this crowding issue.

The adopted aperture corrections for NIRCam bands in Vega magnitudes are the following: F200W:−0.35; F300M: −0.48; F335M:−0.52; and F360M:−0.54. In principle, these values should depend on distance. However, as shown in S. Deger et al. (2022, see their Figure 15), the dependence is quite weak and uncertain; hence, a single set of values has been used for all of the galaxies in the current study. For comparison, the aperture corrections derived with the typical median approach are the following: F200W: −0.64; F300M: −0.67; F335M: −0.77; and F360M: −0.78. The difference between these approaches is approximately 0.2–0.3. When median sky value-derived aperture corrections are applied, there is a clear "offset" between HST fluxes and NIRCam fluxes, where it appears there is a jump in flux between the overall brightness and shape of the NUV-optical SED, and the NIR SED that does not align with any combination of stellar, gas, and dust models. When the 12–20 pixel method is used, this offset is minimized significantly. There is also a difference between the 12 and 20 pixel aperture corrections when the method is implemented on old globular clusters to derive aperture corrections, which are generally Class 1 clusters, and when the method is implemented on only intermediate-age clusters, which are a mix of Class 1 and 2. The aperture corrections derived from only intermediate-age clusters are F200W: −0.36; F300M: −0.37; F335M: −0.36; and F360M: −0.33, which are more uniform and on average 0.1 mag smaller than those derived from globular clusters. This likely indicates that the intermediate clusters are physically less extended than globular clusters. We chose to adopt the 12–20 pixel aperture corrections derived from globular clusters rather than intermediate-age clusters or an average of the two, because it is most consistent with the method by which aperture corrections were derived for HST filters, which were also determined using a population of globular clusters.

3. Modeling Clusters with CIGALE SED Fitting

The goal of this modeling effort is to accurately determine the age, reddening, and mass of each star cluster by comparing their measured photometry with predictions for how clusters evolve over time. Previous works that have used the five broadband PHANGS-HST filters for this purpose (J. A. Turner et al. 2021, S. Deger et al. 2022) have a number of shortcomings (B. C. Whitmore et al. 2021, D. A. Thilker et al. 2022, 2025). In this work, we add Hα and four-band NIRCam infrared photometry to the five broadband NUV-optical filters that have been used previously. We use the Code Investigating GALaxy Emission (CIGALE; M. Boquien et al. 2019) modeling software, described below, incorporating stellar emission, dust attenuation, nebular emission, and dust emission modeling components.

Table 2
CIGALE SED Modeling Parameters for All Grids

Parameter	Notation	Values
`bc03` G. Bruzual & S. Charlot (2003) stellar library		
Metallicity	`metallicity`	See Table 3
Initial mass function (G. Chabrier 2003)	`imf`	1
`sfh2exp` Double exponential SFH		
e-folding (Myr) time of main stellar population model	`tau_main`	0.001
Age of cluster (Myr)	`age`	See Table 3
`dustextPHANGS` Dust extinction curve		
Filters used in fit	`filters`	HST: see Table 1; JWST: F200W, F300M, F335M, F360M
Dust attenuation at 550 nm	`A550`	See Table 3
`dl2014` B. T. Draine et al. (2014)		
Polycyclic aromatic hydrocarbon (PAH) dust mass fraction $q_{\rm PAH}$	`qpah`	[0.47, 0.55, 0.75, 0.95, 1.12, 1.4, 1.77, 3.19, 3.8]
Minimum radiation field $U_{\rm min}$	`umin`	10
Power-law slope $dM_{\rm dust}/dU \propto U^{-\alpha}$	`alpha`	See Table 3
Dust mass fraction heated between $U_{\rm min}$ and $U_{\rm max}$	`gamma`	See Table 3
`nebular` A. K. Inoue (2011), P. Theulé et al. (2024)		
Ionization parameter	`logU`	−3.0
Gas metallicity	`zgas`	0.02
Electron density (cm^{-3})	`ne`	100
Lyman continuum escape fraction	`f_esc`	See Table 3
Lyman continuum dust absorption fraction	`f_dust`	0.0
Emission line width (km s^{-1})	`lines_width`	300.0

3.1. The CIGALE Modeling Framework

CIGALE builds synthetic spectra using multiple component models and generates grids of these models based on input parameters. The component models and their parameters adopted in this work are shown in Tables 2 and 3. It compares the photometry of a cluster with each model in the grid and calculates its χ^2 value. It performs χ^2 minimization, and physical properties and modeled fluxes of the best fit are outputted. While CIGALE also estimates physical properties from the likelihood-weighted means of parameters in the fixed grid of models, doing so results in some edge-of-grid effects that are undesirable when a cluster has a multipeaked probability distribution function. CIGALE operates on the principle of energy balance: the amount of starlight attenuated by dust is completely re-emitted in longer wavelengths. To build the models, CIGALE implements component models in the following order: Stellar populations are synthesized first, and then dust absorption and re-emission is modeled. Finally, nebular emission is modeled based on the dust-affected SED.

We are most interested in constraining the age, mass, and dust attenuation of star clusters. While other parameters vary as described in Tables 2 and 3 and careful consideration goes

Table 3
CIGALE SED Fitting Priors for Cluster Subpopulations

Intended Population	J. A. Turner et al. (2021)	General	Young, Gas- and Dust-rich	Old/Globular
Observational marker	N/A	N/A	Hα EW $>$ 80 Å	D. A. Thilker et al. (2025)
Metallicity	0.02	0.02	0.02	0.0004
Age	[1:10] Myr with $\Delta T = 1$ Myr; [11:13750] Myr with $\Delta \log(T/\mathrm{Myr}) = 0.3$	Same as J. A. Turner et al. (2021)	Same as J. A. Turner et al. (2021)	[1000:13700] Myr, same sampling as J. A. Turner et al. (2021) between 1 and 13.7 Gyr
Dust attenuation	$E(B-V) = [0{:}1.5]$ mag; $\Delta = 0.01$ mag; $R_V = A_V/E(B-V) = 3.1$	A550 = [0:30.0] mag; 100 log-spaced values; $R_V = 3.1$	Same as General grid	A550 = [0:1.0] mag; 100 log-spaced values; $R_V = 3.1$
alpha	N/A	2.0	[2.0, 2.1, 2.2, 2.3, 2.4, 2.5]	2.0
gamma	N/A	[0.0, 0.3, 1.0]	1.0	0.0
f_esc	1.0	1.0	[0.5:1.0] with $\Delta = 0.1$	1.0

Note. All parameters are defined in Table 2.

into defining their parameter spaces, these other parameters' modeled values are evaluated for physical plausibility rather than an expectation of a high degree of precision and accuracy.

3.1.1. Initial Near-ultraviolet-optical Broadband SED Fitting

In initial work using HST broadband photometry (J. A. Turner et al. 2021), two free parameters were allowed: age and reddening. Only stellar continuum emission and dust attenuation modeling components were included, reflecting the lack of direct gas emission data at that time. Stellar models were based on the population synthesis models of G. Bruzual & S. Charlot (2003), hereafter BC03, and a nearly instantaneous star formation burst in which the entire stellar population is born in an interval of 1 Myr, which effectively means clusters were modeled as single-age stellar populations. The BC03 stellar models were adopted because they appeared to show a good match to the observed $U-B$ versus $V-I$ colors of clusters, and had been adopted by previous PHANGS work. The dust attenuation model was based on J. A. Cardelli et al. (1989). An age grid from 1 Myr to 13.75 Gyr, and a reddening grid of $E(B-V)$ from 0–1.5 mag were used. Table 3 describes the specific sampling used in J. A. Turner et al. (2021) in Column (2). All clusters were modeled with solar metallicity ($Z = 0.02$).

Cluster mass is also determined by CIGALE, and depends on the distance to a cluster's host galaxy, intrinsic (extinction-corrected) cluster luminosity, and the assumed IMF. The IMF is assumed to follow a G. Chabrier (2003) distribution from 0.1–100 $M_{\odot}$ and is fully sampled. Full details of the age, reddening, and mass results of the original PHANGS-HST SED fitting method (based on the five broadband near-ultraviolet-optical filters) are given in J. A. Turner et al. (2021).

In this work we continue to use the same BC03 stellar model and dust attenuation model, but modifications have been made to other modeling elements that are described in Section 3.1.2.

Since the completion of that work, a few weaknesses in the age-dating results have been identified. B. C. Whitmore et al. (2021) found that when old, metal-poor globular clusters were fit with solar metallicities, they generally were modeled with young ages and high reddening values, with almost no clusters modeled as having ages and reddening consistent with old globular clusters. They demonstrated the necessity of modeling old globular clusters with subsolar metallicity in order for modeling to result in appropriate ages and reddening.

The degeneracy between age, reddening, and metallicity is multidimensional. When we allow both solar and subsolar metallicities as options for all clusters, the results do not align with established proportions of old globular clusters to other populations. We need to identify old globular clusters before modeling them with appropriately subsolar metallicity. D. A. Thilker et al. (2025) developed a robust method to distinguish between truly young reddened clusters and old globular clusters, detailed in Section 4.3, using Hα emission to identify young reddened clusters and utilizing morphological classification, location in galaxy, and color–color cuts to identify old globular clusters. We adopt many elements of this old globular cluster identification method in this work.

We utilize a fixed solar metallicity for clusters not identified as globular clusters. K. Kreckel et al. (2019) examined the metallicity gradients for eight PHANGS galaxies, and B. Groves et al. (2023) further studied the radial dependence of metallicity in H II regions in 20 PHANGS galaxies with MUSE spectra. Generally, the metallicity gradients observed in this galaxy sample are mild (Figure 10 of that work). Of the galaxies we use in this work, only IC 5332 (38% decrease in metallicity from center to outer edge), NGC 7496 (40% decrease), and NGC 1365 (30% decrease) exhibit significant gradients. The next lower metallicity below solar in the BC03 models is two-fifths solar. Since the large majority of galaxies in this work have much milder radial gradients, and the most extreme galaxies do not get down to two-fifths solar metallicity, using solar metallicity for nonglobular clusters is the most appropriate option of those available in the BC03 library.

The BC03 stellar population models for 1–3 Myr clusters have nearly identical $U-B$ versus $V-I$ colors, leading to a large overdensity of clusters fitted as 1 Myr with high reddening and a relative lack of clusters modeled as slightly older (2–5 Myr) when only near-ultraviolet-optical broadband filters are used. B. C. Whitmore et al. (2025) conducted a morphological study of gas and dust emission surrounding star clusters, focusing on the first 10 Myr, and found that gas (Hα) and polycyclic aromatic hydrocarbon (PAH; 3.3 μm and 7.7 μm) emission are primarily associated with the youngest (1–3 Myr) clusters. They determined star cluster ages both by Hα bubble size, and with $U-B$ versus $V-I$ locations that have little to no issues with age–reddening degeneracy. Figures 5–6 in that work show samples of clusters which are 1–5 Myr, and their surrounding Hα, 3.3 μm and 7.7 μm emission, and while 1–3 Myr clusters generally exhibit Hα and PAH emission that would fall within a 4 pixel HST aperture, 4+ Myr clusters have evacuated their immediate vicinity and do not exhibit any gas or dust emission within this small aperture. This approach provides a path forward to improve or validate the age determination of young stellar clusters with very similar optical colors.

A large fraction of stellar emission can be absorbed and re-emitted through nebular lines (P. Anders & U. Fritze-v. Alvensleben 2003; B. Groves et al. 2008; M. Boquien et al. 2010; A. E. Reines et al. 2010; R. Orozco-Duarte et al. 2022). Therefore, it is important that we include nebular emission in the CIGALE models. Directly including Hα emission as an observation provides a valuable direct constraint on this nebular emission model component. Overall, the addition of Hα, 2 μm, 3 μm, 3.35 μm (which covers the 3.3 μm PAH feature), and 3.6 μm fluxes to the SED fitting requires updates to the CIGALE modeling effort and setup in order to include emission from the gas and dust associated with young clusters, as described in the next section.

3.1.2. Adding Gas and Dust Emission Models

We add new gas and dust emission modules to CIGALE to model the NUV-optical-NIR SEDs of star clusters. Age and reddening continue to be free parameters in our SED fitting, as they were for the original PHANGS-HST setup (described in J. A. Turner et al. 2021). As mentioned earlier, CIGALE operates on the principle of energy balance, and assumes that all gas and dust emission present in a cluster's SED is cospatial with cluster stars, and emission originates from that cluster's UV photons. One limitation of our current implementation is that dynamical evolution, where gas and dust have been swept out or destroyed due to stellar feedback, is not included. This means that gas and dust modeling will be most accurate when

all gas and dust is found within the aperture, and will suffer somewhat as gas and dust expand beyond the aperture. We discuss this limitation and its impacts on modeling in Section 5. For dust emission, we incorporate models from B. T. Draine et al. (2014; hereafter DL2014), which include a mix of small (PAH) and large (silicate and graphite) dust grains. Dust emission is characterized by four parameters: (1) the dust mass fraction of PAH grains ($q_{\rm pah}$), (2) the minimum radiation field ($U_{\rm min}$), (3) power-law slope (α), and (4) the dust mass fraction heated by photons from $U_{\rm min}$ to $U_{\rm max}$ or, in other words, the mass fraction of dust associated with star-forming regions (γ).

For the $q_{\rm pah}$ parameter, we adopt a range of values from 0.47%–3.8% of the dust mass. The values of 0.47, 1.77, 3.19, and 3.8 are included in the DL2014 models, and we have interpolated the values between 0.47 and 1.77. We discuss the observational and theoretical motivation for this interpolation more extensively in Section 5, but in short, a comparison of the size of the observed 3.3 μm PAH feature in the dustiest clusters with the strongest Hα emission in our sample with a wide range of parameter combinations in the DL2014 dust models, indicates that these low values are necessary to best model young HST-identified clusters on a small scale. The resulting $q_{\rm pah}$ values should only be interpreted to represent the strength of the 3.3 μm feature, rather than all PAHs. Past studies of $R_{\rm PAH}$ using MUSE-resolution nebular catalogs (J. Chastenet et al. 2023; O. V. Egorov et al. 2023; J. Sutter et al. 2024) have found the lowest $R_{\rm PAH}$ fractions in H II regions, despite their kiloparsec-scale resolution. Our higher resolution means that very little, if any, diffuse ISM emission is included in measurements of star clusters in the PHANGS catalog.

The α, γ, and $U_{\rm min}$ parameters are described in Equation (23) of B. T. Draine et al. (2007), where U is described by a delta function and a power-law distribution for $U_{\rm min} < U < U_{\rm max}$, and $U_{\rm max}$ is fixed at 10^7:

$$\frac{dM_{\rm dust}}{dU} = (1-\gamma)M_{\rm dust}\delta(U-U_{\rm min}) + \gamma M_{\rm dust}\frac{(\alpha-1)}{U_{\rm min}^{1-\alpha}-U_{\rm max}^{1-\alpha}}U^{-\alpha},\ \alpha \neq 1, \quad (3)$$

where $dM_{\rm dust}$ is the mass of dust heated by starlight intensities in $[U, U+dU]$, $M_{\rm dust}$ is the total mass of dust, $(1-\gamma)$ is the fraction of the dust mass that is exposed to starlight intensity $U_{\rm min}$, and α is a power-law index. Put simply, α represents the steepness of the distribution of dust mass exposed to various starlight intensities.

Typically, $\alpha = -2$ is adopted when studying large chunks of ISM (see also D. A. Dale et al. 2014). γ varies depending on the stellar populations in question, with $\gamma = 1$ being appropriate for the youngest stellar populations (indicating that all dust is being exposed to intense stellar radiation), and $\gamma = 0$ for older stellar populations, where we can assume that no dust is being exposed to intense stellar radiation from massive young stars. The α and γ parameters we adopt vary depending on the star cluster subpopulation being modeled. We adopt $U_{\rm min}$=10 for young clusters capable of creating significant Hα emission within our small aperture, since they should also be capable of heating dust into the NIR regime. A relatively high value of $U_{\rm min}$ is also consistent with our γ constraint since essentially 100% of starlight originates from "star-forming regions" (the clusters themselves) at very young ages.

We incorporate predictions for nebular line and continuum emission based on the models from P. Theulé et al. (2024). The parameters and their values can be found in Table 2. Because nebular emission is generated by young, massive stars within H II regions, we adopt values consistent with young stellar cluster populations. The $f_{\rm esc}$ parameter represents the fraction of Lyman continuum photons that escape the region without being absorbed and re-emitted by gas. Because our star cluster sample was selected from the V-band images, which are dominated by stellar emission, we expect relatively high escape fractions of ionizing photons. Studies of diffuse ionized gas outside of H II regions (M. S. Oey et al. 2007; M. Chevance et al. 2020; F. Belfiore et al. 2022) have found upper limits of $f_{\rm esc}$ in the diffuse ionized gas to be around 0.5. Our young clusters are within H II regions and are optically identified. Since our cluster selection method eliminates many heavily reddened clusters that would see a larger fraction of Lyman continuum photons absorbed and re-emitted, we adopt a minimum $f_{\rm esc} = 0.5$ for our young gas-rich clusters, and allow for a range up to $f_{\rm esc} = 1.0$. Adopting a grid of values up to 1 enables clusters that have blue optical colors and strong Hα emission to be modeled with appropriately young ages. When $f_{\rm esc}$ is fixed at lower values, clusters that are young, have strong Hα, and have bluer optical colors tend to be forced to older ages, when a younger age and higher escape fraction aligns better with analysis of their gas and dust morphology (including the presence of bubbles, nearby objects, etc.), SEDs, and color–color locations. The use of a grid for $f_{\rm esc}$ in clusters with Hα emission allows clusters with lower amounts of gas and dust to be appropriately modeled at the youngest (1–3 Myr) ages. This observationally based parameter grid does mean that we must set $f_{\rm dust} = 0$. CIGALE takes into account the escape fraction and fraction of Lyman continuum photons absorbed by dust by correcting by a factor:

$$k = \frac{1 - f_{\rm esc} - f_{\rm dust}}{1 + \frac{\alpha_1}{\alpha_B} * (f_{\rm esc} + f_{\rm dust})} \quad (4)$$

where α_B = 2.58e−19 m^3 s^{-1} and $\alpha_A - \alpha_B = \alpha_1$ = 1.54e−19 m^3 s^{-1} (G. J. Ferland 1980). In practice, all possible combinations of $f_{\rm esc}$ and $f_{\rm dust}$ in CIGALE inputs must sum to 1 or less. While there is nothing forbidding a user from including combinations that sum to >1, when CIGALE constructs grids of all combinations of parameters, currently any combinations that sum to >1 cause the given modeling run to fail. We plan to implement functionality improving the handling of combinations of $f_{\rm esc}$ and $f_{\rm dust}$ in the future. For all other cluster populations, we adopt a fixed value of $f_{\rm esc}$ = 1.0.

Since the PHANGS galaxy sample focuses on the inner regions of spiral galaxies rather than the outskirts, we adopt a solar gas metallicity (B. Groves et al. 2023). We adopt $\log U = -3.6$, and electron density $n_e = 10$ cm^{-3}, in line with the PHANGS-MUSE analysis of H II regions (A. T. Barnes et al. 2021, 2022; B. Groves et al. 2023).

3.2. Grid Setup and Decision Making

Recent works have shown that cluster age-dating results are improved when appropriate priors are assigned to clusters, and that clusters with different characteristics require different priors (e.g., B. C. Whitmore et al. 2023; D. A. Thilker et al.

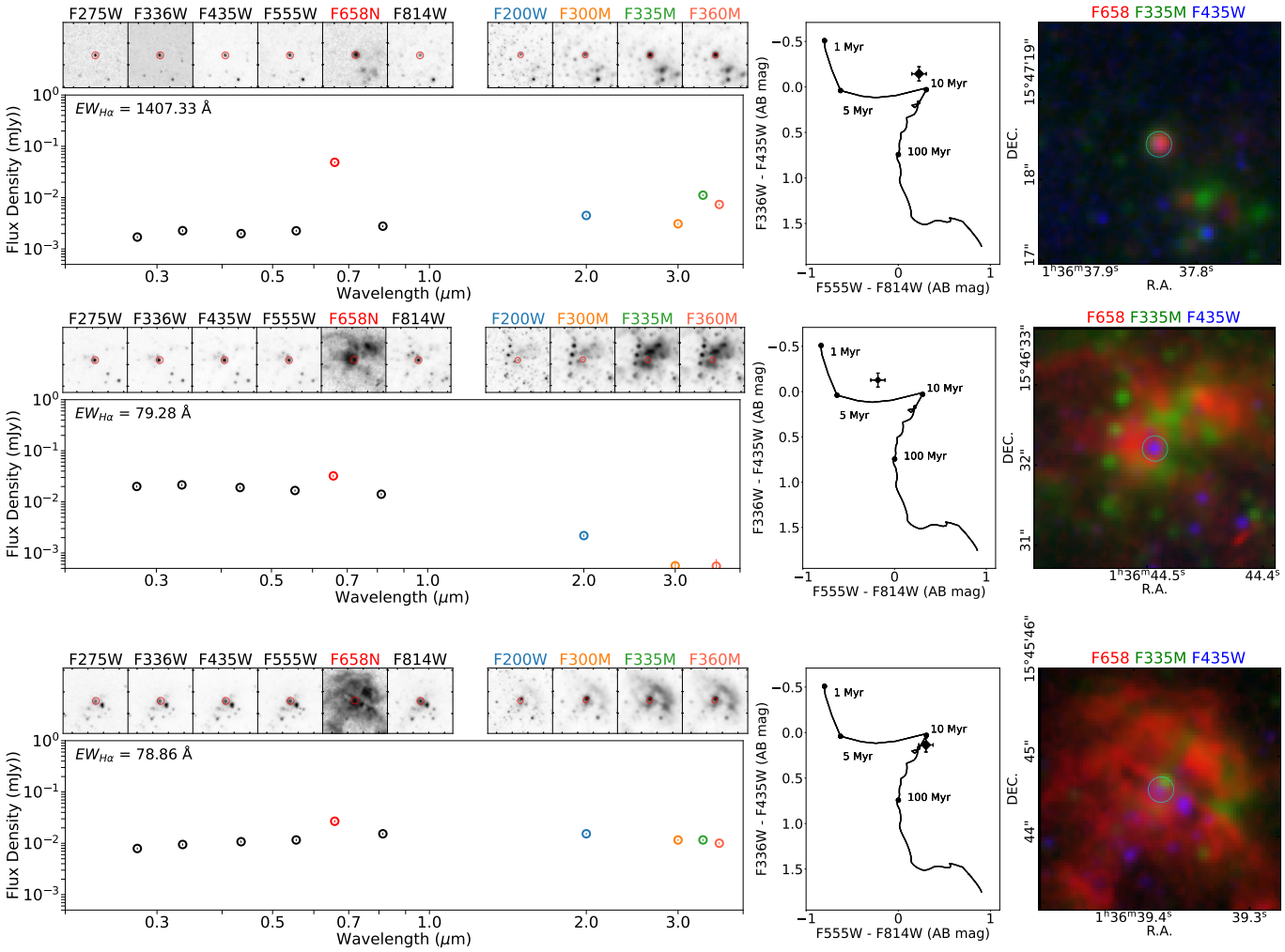

Figure 1. Representative clusters of three broad categories of clusters with moderate-to-strong EW(Hα). Red circles in single-filter cutouts and cyan circles in the RGB cutout show actual aperture size used to perform photometry in each filter. Top panels: a young, reddened cluster with both strong, concentrated Hα and near-infrared dust emission, including a 3.3 μm PAH emission. Middle panels: a young, blue, exposed cluster that has moderate EW(Hα) just below the threshold of 80 Å, and a steep drop-off in the near-infrared. Bottom panels: a cluster with moderate Hα, but a declining near-infrared slope and no sign of a 3.3 μm PAH feature. The cluster is in a strong H II region, and is very closely neighbored by a near-infrared-bright object on the edge of the aperture. Its moderate Hα is not mirrored with near-infrared dust emission, indicating that it may be an older cluster with coincident, unrelated diffuse Hα emission.

2025). In this section we describe the three different sets of priors and corresponding model components used in this work, and how clusters are assigned to the most appropriate set of priors for modeling. The three broad categories of clusters that require distinct priors are:

1. "Young, gas-rich (YGR)": young HST-detected (at least three broadband filters including F555W) clusters with abundant Hα, which may be moderately but not heavily embedded.
2. "Old/Globular Cluster (OGC)": old or globular clusters with subsolar metallicity and little-to-no dust.
3. "General": solar-metallicity clusters with little-to-no gas or dust.

We select which of these grids is most appropriate for each cluster based on its Hα EW (YGR), and a multifaceted color–color, morphology and location-based set of criteria to identify OGCs, each detailed in their respective sections below. Table 3 describes the specific priors used to fit the SEDs for each of our three populations. The following sections discuss the motivations for each set of priors.

3.2.1. Young, Gas-rich (YGR) Grid

Very young clusters, where warm ionized gas and hot dust emission dominate the narrowband Hα and near-infrared filters (P. Anders & U. Fritze-v. Alvensleben 2003; B. Groves et al. 2008; M. Boquien et al. 2010; A. E. Reines et al. 2010), require models that include the gas and dust emission described in the previous section. These clusters are typically moderately reddened with $E(B-V) \gtrapprox 0.15$ mag, and much of the ultraviolet radiation from cluster stars is absorbed and re-emitted in hydrogen recombination lines such as Hα and Paα, and NIR dust emission. We do not expect to find heavily reddened clusters in our catalog, as they are unlikely to have photometric measurements in enough HST broadband filters (at least three-fifths, including the F555W band) to be included in the cluster catalogs, but we do allow for $E(B-V)$ values up to 10 mag to accommodate this possibility.

To determine a threshold for EW(Hα) above which a cluster would be most appropriately fit with nebular emission, we visually inspected all clusters in several galaxies (NGC 628c, NGC 1672, NGC 3351) using a multifaceted diagnostic as shown in Figure 1.

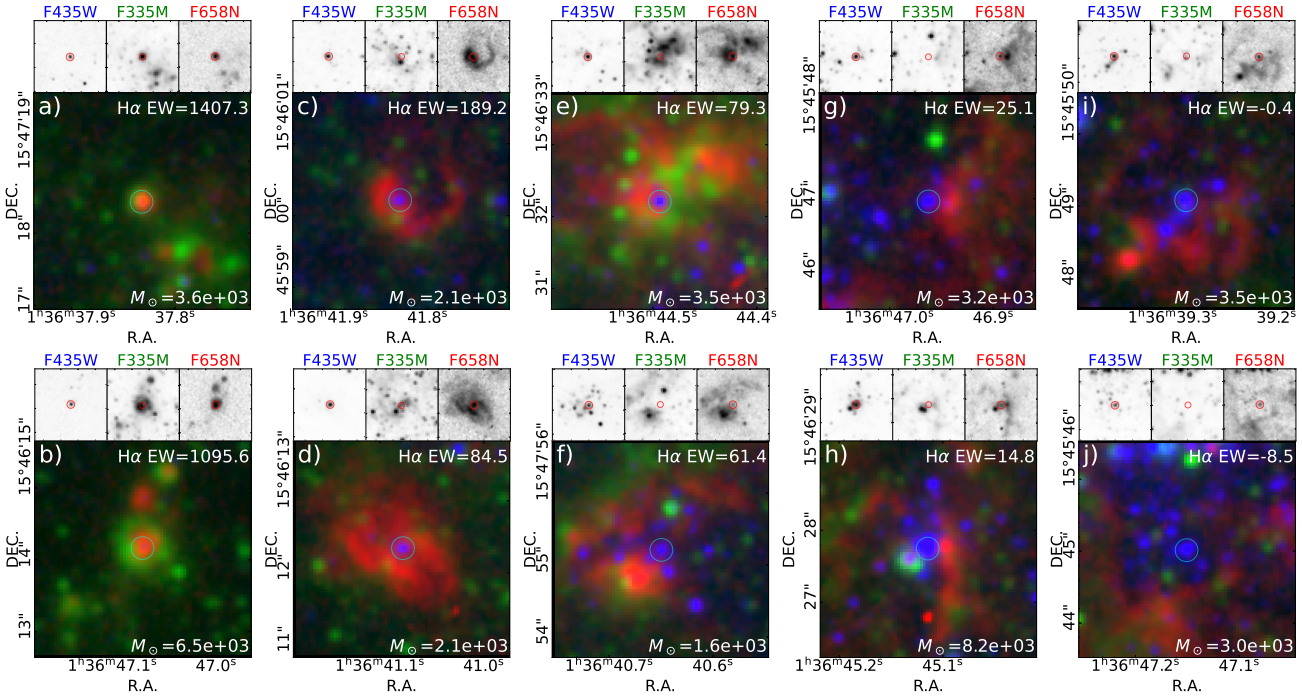

Figure 2. Clusters with a range of Hα equivalent widths, with strongest EW on the left, and weakest on the right. Clusters (a) and (b) have very strong Hα emission and a correspondingly high EW, clusters (c) and (d) have moderate Hα that may still affect SED fitting, clusters (e) and (f) have Hα just below the threshold of 80 Å, clusters (g) and (h) have very low Hα EW, and clusters (i) and (j) functionally have no Hα emission. Note that moving from left to right, Hα morphology expands, and extended 3.3 μm emission indicative of hot dust is found outside of Hα bubble perimeters when it is present.

Figure 1 illustrates three broad categories of clusters that show Hα emission above the stellar continuum. The cluster in the top panel is young and reddened, with a very strong EW(Hα), and requires nebular emission (continuum and lines) to be modeled correctly. The cluster in the middle panel has a lower EW(Hα), has a blue optical and near-infrared SED, and is located in an active star-forming region. It is also relatively high above the G. Bruzual & S. Charlot (2003) stellar continuum track shown in $U-B$ versus $V-I$ space (black point in the center subfigure of each panel). All of these things indicate that it is young but exposed, and does not require nebular emission to find an appropriate age, mass, and reddening. The cluster in the bottom panel has a very similar EW(Hα) as the middle cluster. However, this cluster's moderate Hα is not mirrored by near-infrared dust emission within the aperture, as we can see in the RGB image in the left subfigure, indicating that its red optical slope is likely the result of an older (>5 Myr) age rather than significant reddening of a very young cluster, and its Hα emission is diffuse.

Using NUV-near-IR SEDs, $U-B$ versus $V-I$ colors, and both gas and hot dust morphology, we determined a threshold for the inclusion of nebular emission of EW(Hα) > 80 Å . The middle and bottom clusters in Figure 1 illustrate the reasoning behind setting this EW threshold: generally, clusters with EW(Hα) around 80 Å exhibit diffuse gas emission, and their Hα is a much less reliable predictor of cluster-originating gas and dust emission than clusters with higher EW(Hα). The origin of Hα emission is often unclear for clusters with EW(Hα) < 80 Å: it may be energized by photons from the star cluster we are modeling, but it may also be energized by photons from another star cluster or association nearby. Thus, the strength of Hα for clusters with more diffuse emission, corresponding to an approximate EW(Hα) < 80 Å does not necessarily reflect how much of their output is going into nebular line emission. The YGR designation is meant to identify only clusters for which nebular emission is *required* for reasonably accurate modeling, rather than identifying all clusters that have Hα above the continuum, or all clusters within H II regions.

The various levels of Hα proximity to and in association with young star clusters are illustrated in Figure 2. We show a selection of clusters representing various levels of Hα emission, with the highest Hα emission on the left, and the lowest on the right. All clusters except those with EW > 1000 Å are within the L-shaped "basket" formed by the 1–10 Myr portion of the BC03 stellar continuum track. Moving from right to left, we see the gas and dust morphology of clusters expand well beyond our aperture size, with hot dust/small PAHs generally existing outside of Hα emission.

In Section 4.2.1 we discuss EW(Hα) < 80 Å "weak" Hα emitters that fall below the EW threshold (such as clusters (e) and (f) in Figure 2), and modeling continuity between clusters above the Hα EW threshold deemed to require nebular emission and those below the threshold that are deemed not to require it.

Clusters with a measured EW(Hα) > 80 Å are modeled with the young, gas-rich SED fitting grid. As described above, examination of many clusters with EW(Hα) > 80 Å in a 4 pixel radius aperture shows that Hα emission is directly associated with the clusters rather than being diffuse or emission that originates from a larger H II region created by nearby star formation. Clusters above this EW(Hα) threshold are very likely to be impacted by nebular emission. In the most embedded cases in our catalog, Hα emission is detected even when most other HST bands are upper limits. These embedded clusters have EW(Hα) well above our threshold, making this

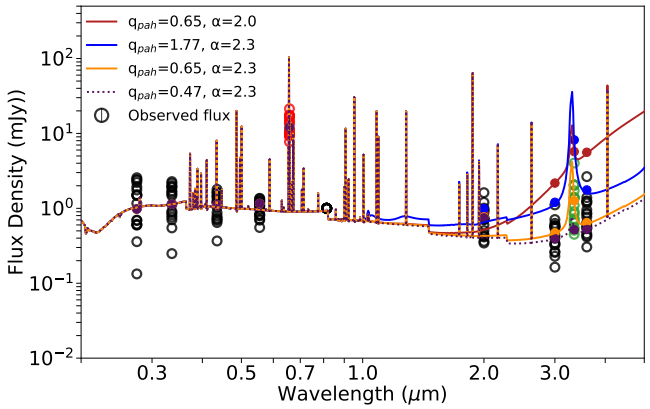

Figure 3. NUV-optical-NIR SED showing the strongest Hα emitters in NGC628c, all with Hα EW $>$ 500 Å (open circles), and four example models. All example models are for a 1 Myr cluster with $f_{\rm esc} = 0.8$ and $A_{550} = 1.0$. Both observations and models are normalized to the F814W band. Note that these clusters generally do not show an increasing NIR slope from the 2 to the 3 μm filter.

criterion also effective for identifying more heavily reddened clusters as long as Hα can be detected.

We found that the NIR SED shapes created with $q_{\rm PAH}$ and α values included in the DL2014 models and most commonly used for lower-resolution studies of the ISM are not consistent with the observed NIR SED shapes of our most dusty clusters. Figure 3 shows the observational SEDs of the most Hα-bright, dusty clusters in NGC 628c with Hα EW $>$ 500 Å (much higher than our threshold, and generally compact) and three selected models that illustrate this. When comparing the first model (red) to observations, we can see that the NIR slope between the 2 μm and 3.6 μm filters in observed clusters does not rise continually, as is the case for a model with $\alpha = -2.0$. The models with $\alpha = 2.3$ on the other hand, have an NIR SED slope that is compatible with our super gas and dust-rich clusters. We can also see that with an α value that reflects the NIR SED shape of observed clusters, even the relatively low $q_{\rm PAH}$ value of 1.77 exhibits a PAH feature that is much larger than the size of the PAH feature of the observed clusters, and still has a steadily increasing NIR SED slope between the 2 μm, 3 μm, and 3.6 μm bands, which is not reflected by observed clusters. A model with a lower $q_{\rm PAH}$ value of 0.65 and $\alpha = 2.3$ (orange), on the other hand, reflects both the overall NIR shape, and the size of the 3.3 μm PAH feature. If given only the choice between the lowest $q_{\rm PAH}$ value included in DL2014 (0.47, shown as the dotted line in purple) and the next larger value of 1.77, neither is a good fit for the behavior of actual gas- and dust-rich clusters in the NIR. These comparisons of the dustiest and most gas-rich clusters in our catalog with models has led us to make the following adjustments to our dust emission modeling parameters, to better reflect the range of characteristics that YGR clusters exhibit.

First, we interpolated several $q_{\rm PAH}$ values between 0.47% and 1.77%, and computed the associated models. These models with interpolated $q_{\rm PAH}$ values align much better with the observed size of the 3.3 μm PAH feature in HST-identified clusters, as shown in Figure 3. Second, we determined that to have a "flatter" near-infrared dust continuum slope reflective of observational SEDs, larger α values are needed, and we allow α to be a free parameter between [−2.0, −2.5]. YGR clusters with dust emission generally are best fit by slightly

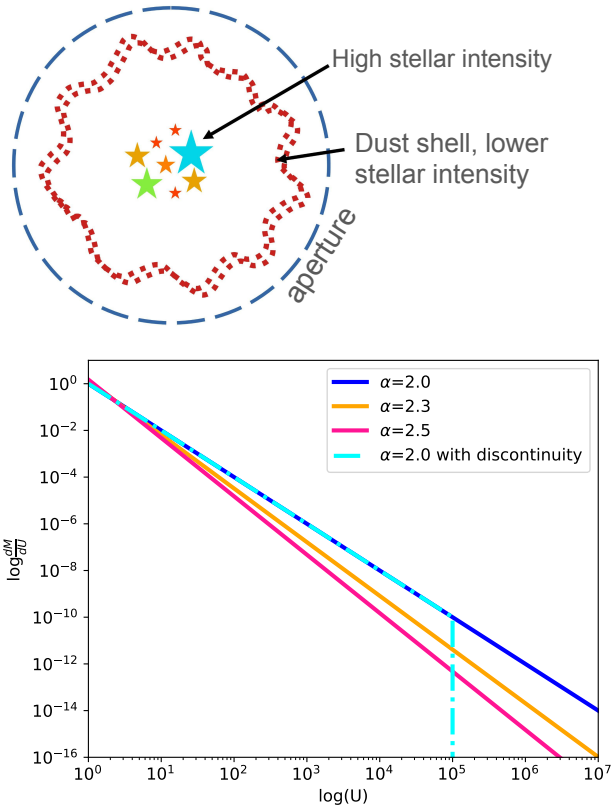

Figure 4. Top panel: a young star cluster that has begun forming a dust bubble that is not yet big enough to be resolved with NIRCam, and whose bubble is not yet big enough to extend beyond a small aperture. Bottom panel: various continuous dust mass heating scenarios (solid lines) plus an approximately truncated situation as schematically portrayed in the top panel.

larger α values between −2.2 and −2.4. An illustration of one possible reason for the need for larger α values is shown in Figure 4. We observe many clusters that have clearly identifiable photodissociation regions (PDRs), where dust emission is brightest outside of an Hα bubble, and outside our 4 pixel aperture. We would expect that clusters that are forming PDRs that are still smaller than our aperture are also in our catalog, illustrated in the top panel of Figure 4. Since these clusters have already partially blown out their dust, no dust would remain close enough to the cluster to be heated by the highest stellar intensities. The bottom panel shows the effect this scenario would have on the distribution of dust mass exposed to various stellar intensities: the lack of dust very close to the cluster would cause an approximate discontinuity in the distribution of dust mass heating, which would be best fit by a larger α value. This treatment of α demonstrates the inherent limitations in using a dust emission model that does not incorporate dynamical elements.

Overall, 14% of the clusters in our sample were assigned to the YGR grid via their Hα EW, with a range of 6%–28% of clusters being assigned to the grid in individual galaxies. Table 4 shows a breakdown of the number of YGR-designated clusters in each galaxy.

3.2.2. Old Globular Cluster Grid

Ancient globular clusters have subsolar metallicities. When solar metallicity is adopted for an entire cluster population, as was done in the initial PHANGS-HST modeling approach

Table 4
Number of Clusters in Each Grid for All Galaxies

Galaxy	Total	YGR (%)	General (%)	OGC (%)
IC 5332	166	42 (25)	104 (63)	20 (12)
NGC 628c	295	37 (13)	205 (69)	53 (18)
NGC 628e	25	7 (28)	17 (68)	1 (04)
NGC 1087	482	67 (14)	366 (76)	49 (10)
NGC 1300	257	57 (22)	135 (53)	65 (25)
NGC 1365	558	34 (06)	401 (72)	123 (22)
NGC 1385	503	47 (09)	393 (78)	63 (13)
NGC 1433	173	27 (16)	94 (54)	52 (30)
NGC 1512	220	57 (26)	108 (49)	55 (25)
NGC 1566	623	112 (18)	450 (72)	61 (10)
NGC 1672	353	65 (18)	258 (73)	30 (08)
NGC 3351	163	18 (11)	97 (60)	48 (29)
NGC 3627	551	39 (07)	450 (82)	62 (11)
NGC 4254	411	36 (09)	340 (83)	35 (09)
NGC 4303	512	109 (21)	337 (66)	26 (05)
NGC 4321	602	55 (09)	494 (82)	53 (09)
NGC 7496	236	47 (20)	159 (67)	30 (13)

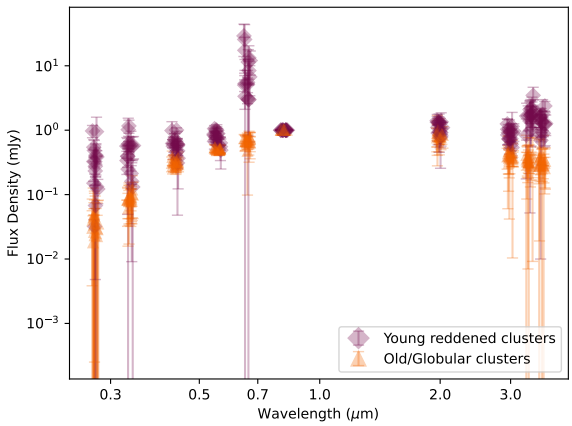

Figure 5. Median SED of each of our 16 galaxies for young, gas- and dust-rich clusters modeled with $A_V > 0.5$ mag (purple diamonds), and for bright old/globular clusters (orange triangles), normalized to the F814W band. A random log-uniform value has been added to wavelength to spread out points at each filter. Without markers of gas and dust, these two populations are easily confused. When we add Hα and near-infrared hot dust emission markers, the populations have distinct shapes, and their identities become distinct from each other.

(J. A. Turner et al. 2021), most globular clusters had catastrophic failures in the best-fit age and reddening (B. C. Whitmore et al. 2023). For example, M. Floyd et al. (2024) found that ≈80% of likely globular clusters had estimated ages that were a factor of 10–1000 times too low when five-band optical broadband photometry was fit by a solar metallicity model.

Here, we identify ancient globular clusters, then age-date them using a set of priors designed specifically to avoid common age-dating problems. To identify old, globular clusters, we use the method laid out by D. A. Thilker et al. (2025), as shown in Figures 3 and 5 of that work. In order to be identified as an OGC, a cluster must either be Class 1, which can be projected to be located anywhere within a galaxy, or Class 2 and located outside of spiral arm masks based on the work of M. Querejeta et al. (2021). It also must fall into an OGC-dominated color–color region in $U-B$ versus $V-I$ space, or B versus $V-I$ color–magnitude space when U-band photometry is not robust. These selection polygons were derived from the color–color density diagrams of the entire PHANGS-HST cluster sample as first presented by D. Maschmann et al. (2024b), by determining contours that isolate the overdensity formed by Class 1 clusters of probable low metallicity, from younger, higher-metallicity clusters. This color–color region selection is described in D. A. Thilker et al. (2025), and was independently validated by transforming Milky Way globular clusters from the Harris catalog (W. E. Harris 2010) into the HST photometric system, then generating mock photometry (color–color diagrams) as if these known GCs were observed at the median distance of PHANGS-HST galaxies.

We fit clusters selected for the OGC grid with 1/50th solar metallicity, an age grid from 1–13.7 Gyr, and $A_{550} < 1$ ($E(B-V) < 0.32$). The addition of NIRCam and HST-Hα greatly improves our ability to distinguish between young, gas-rich clusters and OGCs, as shown in Figure 5, where we can see their drastically different shapes when these filters are added to HST broadband filters. The addition of Hα and near-infrared photometric data clearly distinguishes clusters with and without gas and dust, particularly between young, gas- and dust-rich clusters and the oldest subsolar metallicity globular clusters. Figure 5 shows the median SEDs of the most gas- and dust-rich clusters, and the old globular clusters in each galaxy, normalized to the F814W band. The SED shape of the two subpopulations in five optical broadband filters, while not identical, have a similar declining shape toward shorter wavelengths. Especially in galaxies with a lot of dust (the young points that fully overlap with the globular cluster median SEDs are from NGC 1365, a galaxy with extremely dense dust lanes), classifying a given cluster as being old and red or young and reddened is difficult. However, we can see that there is no overlap between the two different ages when we look at the Hα and 3–3.6 μm data points. Not only do the young clusters have very strong Hα, these clusters also have strong near-infrared dust emission that clearly distinguishes them from old globular clusters.

However, there is still a degeneracy between relatively old (a few 100 Myr) and reddened, and very old low-reddening solutions. Restricting age and reddening can lead to artificial clumping of clusters at the edges of these priors, and so we tested a number of age and reddening restrictions to determine which led to the most reasonable solutions and least edge effects. We tested restricting age only (both >1 Gyr and >10 Gyr), restricting reddening only ($A_{550} < 1.0$, $A_{550} < 0.5$), and all combinations of these restrictions, and found that the prior restrictions of 1–13.7 Gyr, and $A_{550} < 1$ ($E(B-V) < 0.32$) showed the least artificial clumping and greatest assignment of realistically old ages and low reddenings to OGC-flagged clusters.

Overall, 13% of clusters in our sample were assigned to the OGC grid, with a range of 4%–30% of clusters being assigned to the grid in individual galaxies. Table 4 shows a breakdown of the number of OGC-designated clusters in each galaxy.

3.2.3. General Grid

Clusters that do not satisfy the Hα equivalent width requirement for the young, gas-rich grid or the classification, location, and color–color requirements for the OGC grid are fit by the parameters adopted for the general grid.

Clusters that are assigned to the general grid are assumed to be approximately solar metallicity. They do not have enough nebular emission that the nebular model is required to find a good-quality fit, meaning that they are either young but exposed, or older and lacking sufficient UV photons to ionize gas. We do not apply any restrictions on age or reddening. In particular, we do not exclude very old, OGC ages. While our OGC identification method is robust for decontaminating OGC from young clusters, it is possible and reasonable to expect that some true OGCs are incorrectly assigned to the general grid in that process and that with NIRCam's constraint on the near-infrared stellar continuum and dust emission, these clusters may still get OGC ages and reddenings despite modeling them with solar metallicity.

We assign $\gamma = 1$ to our young and Hα-rich clusters, and $\gamma = 0$ to clusters in our OGC grid. An environment with $\gamma = 0$ would be unable to heat dust to the point of detectability with NIRCam, while $\gamma = 1$ is reflective of a region dominated by active star formation where dust can be heated enough that it emits in the near-infrared range. This can be seen in Figure 13 of B. T. Draine et al. (2007): stellar intensities $U > 10^6$ exhibit an elevated NIR continuum with a more minor increase in the 3.3 μm PAH feature strength, whereas lower stellar intensities are heavily dominated in the NIR by PAH feature emission. Since young clusters are the only populations with the massive stars needed to achieve these high stellar intensities, any cluster category that includes young stars should include $\gamma = 1$. The general grid clusters are optically exposed and span a range of ages from very young to middle-aged, to potentially OGCs. Young exposed clusters are capable of intensely heating dust to the point that dust emission is detectable at near-infrared wavelengths within the aperture, so $\gamma = 1$ needs to be included. We also include both $\gamma = 0$ as well as a logarithmically middle value of $\gamma = 0.3$, to reflect the changing proportion of light originating from star-forming regions over a cluster's lifetime as it loses the most-massive stars. We exclude unphysical combinations of age and γ where age is $<$10 Myr and $\gamma = 0$, as this represents a scenario where a cluster has massive young stars but is incapable of heating dust into the NIR. Young clusters in the general grid are generally very exposed, but should be capable of heating dust into the NIR if dust is present.

Overall, 71% of clusters in our sample were assigned to the general grid, with a range of 49%–83% of clusters being assigned to the grid in individual galaxies. Table 4 shows a breakdown of the number of general grid-designated clusters in each galaxy.

3.3. Final Grid Selection

Table 4 compiles the number and percentage of clusters in each of our 17 fields directed to the (1) young, gas-rich grid (YGR), (2) general grid, and (3) OGC grid. In general, galaxies with the highest number of total clusters have the highest fraction (at least 50%) directed to the general grid. The remaining clusters are split between the YGR and OGC grids, ranging from galaxies with many more YGRs than OGCs (NGC 628e, NGC 4303), to galaxies with many more OGCs than YGRs (NGC 1365, NGC 3351). Note that this balance is affected by the inherent selection effects resulting from our cluster identification method: galaxies with well-documented dense dust lanes and embedded sources like NGC 1365 are preferentially less likely to have optically detected young clusters than galaxies with less obscuring dust.

4. Results

In this section, we present the age, mass, and reddening results when all 10 HST+JWST/NIRCam filters are included in SED modeling. We also make a detailed comparison of age, reddening, and mass results with: (1) six HST filters, using the same selection and modeling procedure, (2) the recent work of D. A. Thilker et al. (2025), which uses broadband HST plus Hα (from HST and from ground-based data) with different criteria for grid selection and best-fit processing, and (3) previous PHANGS-HST age estimates based on the five broadband HST filters and a single set of SED fitting parameters for all clusters (J. A. Turner et al. 2021; S. Deger et al. 2022).

4.1. Age, Reddening, and Mass from HST+NIRCam

The mass–age diagrams for clusters in each of our 16 galaxies are shown in Figure 6. The solid line along the bottom edge of the data shows the luminosity limit for the cluster population in each galaxy. These vary for each galaxy and show that our luminosity-limited samples do not include lower-mass clusters at older ages because clusters fade over time as the most-massive stars die off. The composite age–mass diagram in the top-left panel includes clusters from all galaxies and shows that the clusters have a range of ages from $\sim$1 Myr through $\sim$13 Gyr, and a range of masses from $\sim 10^3$to 10^7 $M_\odot$.

Clusters are coded by the grid that was used to age-date them: (i) young, gas-rich grid in purple, (ii) OGC in orange, and (iii) general grid clusters in blue. Overall, clusters that have a sufficiently high EW(Hα) to send them to the YGR cluster grid have modeled ages between 1 and 10 Myr. Clusters sent to the OGC grid must have ages of 1 Gyr and older due to our age priors, but show the highest densities at the oldest ages.

Some clusters fitted with the general grid are modeled with OGC ages and masses, and visual inspection confirms that they are possible OGCs that fall outside of our OGC criteria. Our OGC selection criteria preferentially select isolated OGCs, to reduce potential contamination from younger clusters. As described in Section 3.2.2, to end up in the OGC grid, clusters must either be Class 1, or Class 2 and located outside of the galaxy's spiral arm mask. This means that Class 2 clusters that are located within a galaxy's spiral arm mask are automatically sent to the general grid, even if they have the colors expected of OGC.

We will discuss the OGC color space in more depth in Section 4.2.4. We also see that there is overlap between YGR clusters and young exposed clusters (turquoise, $<$10 Myr), with increasing proportions of exposed clusters with increasing age, until exposed clusters completely dominate at 10 Myr. YGR clusters and young exposed clusters generally span the same mass ranges.

There are a number of interesting features in the modeled age distribution. Cluster ages appear fairly continuous, although there is a pileup at $\approx$100 Myr and a dearth of clusters in the 10–30 Myr range and $\approx$100–200 Myr range. Some gaps are due to the discreet nature of the BC03 models used in the SED fitting (for example, the apparent gaps

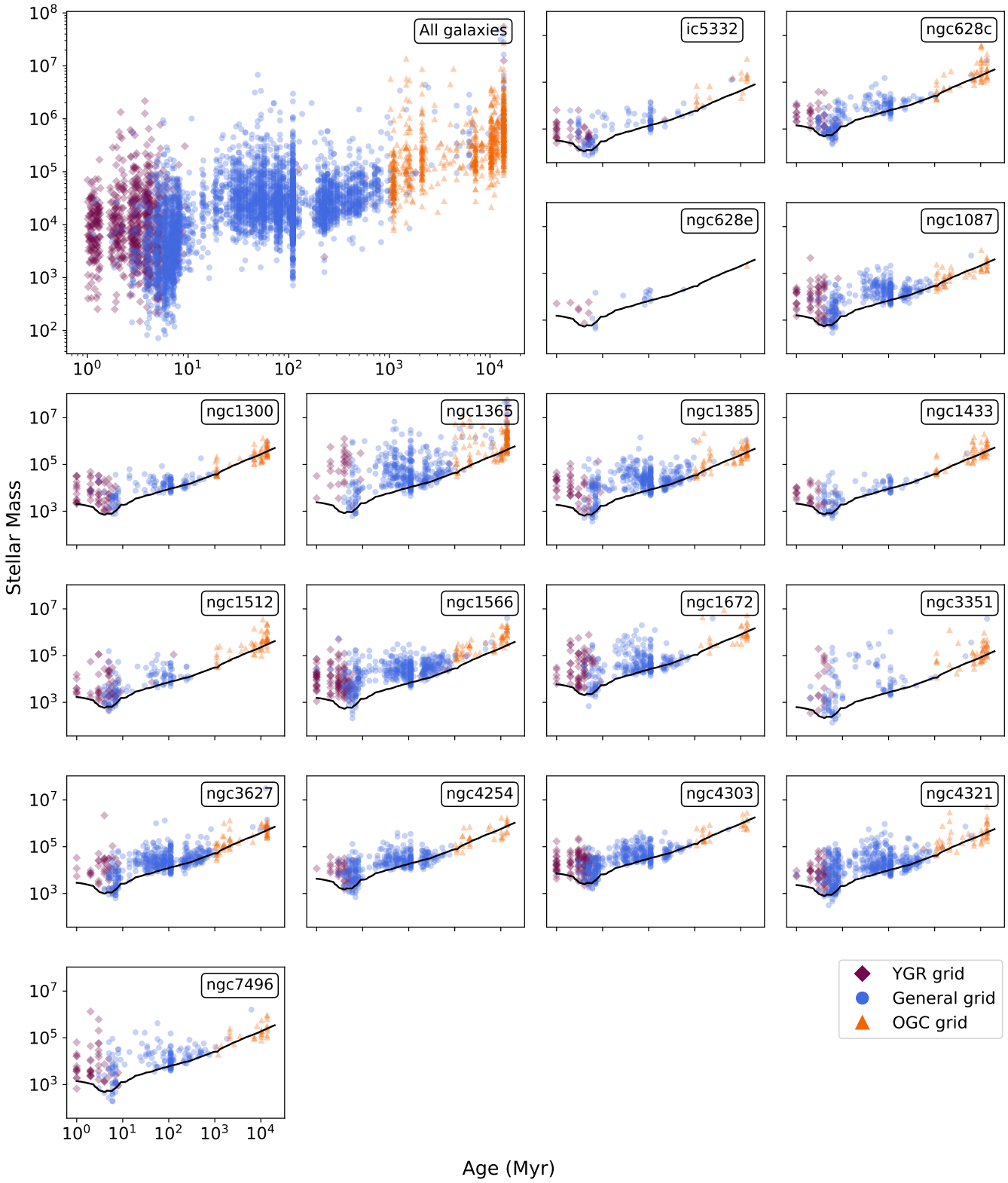

Figure 6. Age–mass distribution for all human-classified clusters in our 16 galaxy sample, fitted with HST broadband, Hα, and NIRCam. Clusters fitted with the young, gas-rich grid are purple diamonds; clusters fitted with the OGC grid are orange triangles; and all other clusters (general grid) are blue circles.

between 1, 2, and 3 Myr, and the gaps at ages >1 Gyr, which result from a coarse sampling of the oldest ages). Others, like the apparent gap between 10 and 20 Myr is due to the BC03 models looping back on themselves in $U-B$ versus $V-I$ color–color space in this age range, predicting a fairly small range of colors over this time period. The ∼100 Myr pileup also results from a feature of the BC03 models in $U-B$ versus F200W $-I$ color–color space (also seen with other NIRCam filters), where the stellar track shows a bend such that several ages fall along the reddening vector, resulting in a sweep-up effect as a large collection of clusters are closest to a single-age model. The number of massive clusters younger than

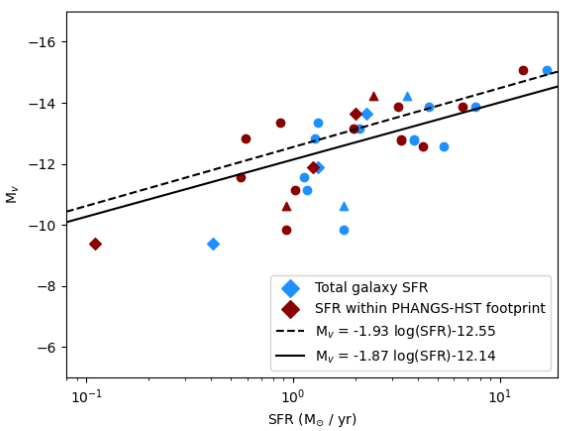

Figure 7. Total galaxy SFR (blue) and SFR within the PHANGS-HST footprint (dark red; A. K. Leroy et al. 2021) vs. M_v of the brightest V-band cluster in each PHANGS-JWST galaxy, and M_v–SFR relations derived by C. Weidner et al. (2004) from a sample of dwarf and spiral galaxies in the local Universe. The dashed line includes all galaxies, and the solid line is after removing four outlier galaxies.

≈few × 100 Myr appears to scale with the current star formation rate—actively star-forming galaxies like NGC 1365 and NGC 1672 have a large number of intermediate-age massive clusters, while galaxies with lower star formation rates like IC 5332 and NGC 1433 have relatively few of these clusters. Figure 7 shows the brightest cluster in the V band in each galaxy versus the galaxy's overall SFR (blue) and the SFR specifically within the PHANGS-HST coverage (dark red; A. K. Leroy et al. 2021), compared with the relations derived by C. Weidner et al. (2004) from a population of dwarf and spiral galaxies at $z \sim 0$, and find there is overall good agreement.

The age–reddening results for 16 galaxies are shown in Figure 8. As in Figure 6, the top-left figure shows the composite of all 16 galaxies, (i) the young, gas-rich grid is shown in purple, (ii) OGCs are in orange, and (iii) the remaining clusters fit by the general grid are in blue. Overall, only the youngest (<10 Myr) clusters show reddening above $E(B-V) \sim 0.5$ mag in significant numbers, despite the fact that for the YGR and general grids, we allowed A_{550} as high as 30 mag and $E(B-V)$ up to ∼10 mag. NGC 1365, the most extreme dust-rich galaxy in our sample, is the biggest source of clusters with modeled values $E(B-V) > 0.5$, in both the YGR and general grids. Given that our cluster sample was identified with HST and required detection in three bands including the V band, this selection effect means we would expect few, if any clusters with $E(B-V) \gtrsim 2$ in our sample.

The YGR clusters are overall younger and more reddened than young, exposed clusters modeled with the general grid. We see a relatively smooth transition from YGR clusters dominating at 1 Myr, to exposed, general grid clusters dominating at 7 Myr, with essentially no YGR clusters >10 Myr. We find that while most very young clusters (1–3 Myr) have enough Hα to require nebular emission in the SED fits, low-reddening and completely exposed clusters do exist at every age from 1–10 Myr. The transition between YGR clusters and young exposed clusters is smoothly handled with our young and general grid parameters.

A distinct feature of the YGR clusters is the presence of a number of clusters with modeled ages of ∼4–5 Myr, and $E(B-V) \geqslant 0.75$. We examined the clusters with these characteristics individually. Note that NGC 1365, which has the highest SFR in our sample, is the source of most of these clusters, and when compared with the predicted star-forming galaxy main sequence at $z = 0$ (B. Catinella et al. 2018; A. K. Leroy et al. 2021; see also Figure 27 of D. A. Thilker et al. 2025), all galaxies that contain clusters with these modeled characteristics exhibit higher-than-average SFRs for their masses. These clusters universally have moderate Hα EW and very steeply red optical slopes, consistent with highly reddened clusters where Hα is attenuated. They are modeled with high masses, most $>10^5 M_\odot$ (which can also be seen in Figure 6), and many lie in or adjacent to visible dust lanes. All of these characteristics are compatible with young, massive star clusters.

These clusters' modeled ages of 4–5 Myr are largely an artifact of the precise shape of the BC03 stellar tracks. If clusters are just a little redder than expected in the BC03 models for reddened 1–3 Myr populations, they will be modeled to the 4–5 Myr part of the models, which has a redder NUV − U − B color than the 1–3 Myr part of the track. If we think in $U-B$ versus $V-I$ color–color space, these clusters are "below" the reddening vector that would take them to the 1–3 Myr tip of the BC03 track. Because of the large uncertainties present in the NUV and U bands for very reddened clusters, their precise SED shapes are unavoidably uncertain as well, leading to these slightly unrealistic ages. Manual verification demonstrates that generally, YGR clusters with modeled $E(B-V) > 0.75$ have characteristics consistent with young, massive, reddened clusters, which are much more likely to be 1–3 Myr than 4–5 Myr. They exhibit condensed Hα emission consistent with clusters that have not yet cleared their natal gas and dust, which for the modeled masses that these clusters exhibit, should be cleared very rapidly. In Figure 6, we can also see a small population of young, massive clusters around 4–5 Myr, which is this same population.

4.2. Comparison with HST Broadband + Hα Results

Figure 9 compares the best-fit age (left), mass (middle), and reddening (right) from our SED modeling, with and without the NIRCam filters. The data are plotted by the number density of clusters. A dashed line represents 1-to-1 values, and parallel solid lines represent results within a factor of 2 of a 1-to-1 result.

Overall, the age results appear to be consistent with and without NIRCam filters, although with significant scatter. We find that 55% of the clusters (2740/6119) have best-fit age results agreeing to within a factor of 2. At the youngest ages <10 Myr, the results show a tighter correlation than that of older ages, although there are notable deviations, which will be discussed in Section 4.2.3. There is more variation (the contours are a bit broader) at ages between 100 Myr and 1 Gyr.

The mass distribution has the greatest spread, with 51% of clusters agreeing to within a factor of 2. Modeling with NIRCam filters generally results in HST+Hα-modeled low-mass clusters decreasing in mass with the addition of NIRCam, and higher-mass clusters increasing in mass with the addition of NIRCam. The $E(B-V)$ distribution has the narrowest distribution, with 80% of clusters agreeing to within a factor of 2. However, the distribution of reddening deviates much further from 1:1 than that of mass or age, with

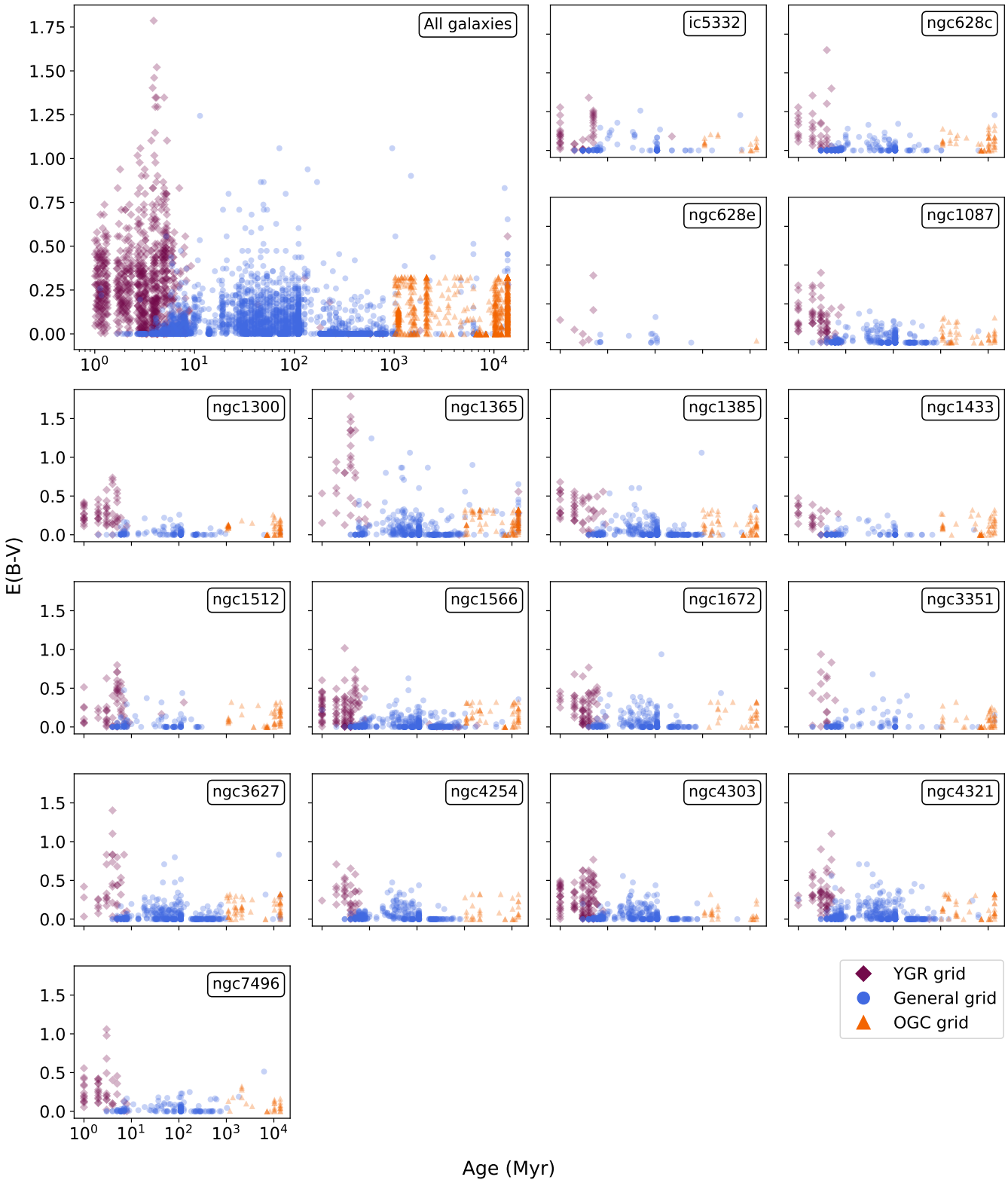

Figure 8. Modeled age–reddening distribution for all human-classified clusters in our 16 galaxy sample, fitted with HST broadband, Hα, and NIRCam. Clusters fitted with the young, gas-rich grid are purple diamonds; clusters fitted with the OGC grid are orange triangles; and all other clusters (general grid) are blue circles.

many clusters modeled as having moderate reddening with only HST+Hα, being modeled with much lower reddening when NIRCam filters are added. Very few clusters are modeled with more reddening when NIRCam is included than when it is not included. The most notable features that deviate from a 1:1 distribution in Figure 9 are the knot of clusters that moved from a young to an older age with the addition of NIRCam data, and the split distribution of $E(B-V)$ where many clusters modeled with higher reddening with HST filters move to very low reddening with NIRCam. We will discuss these features in Sections 4.2.1 and 4.2.2, respectively.

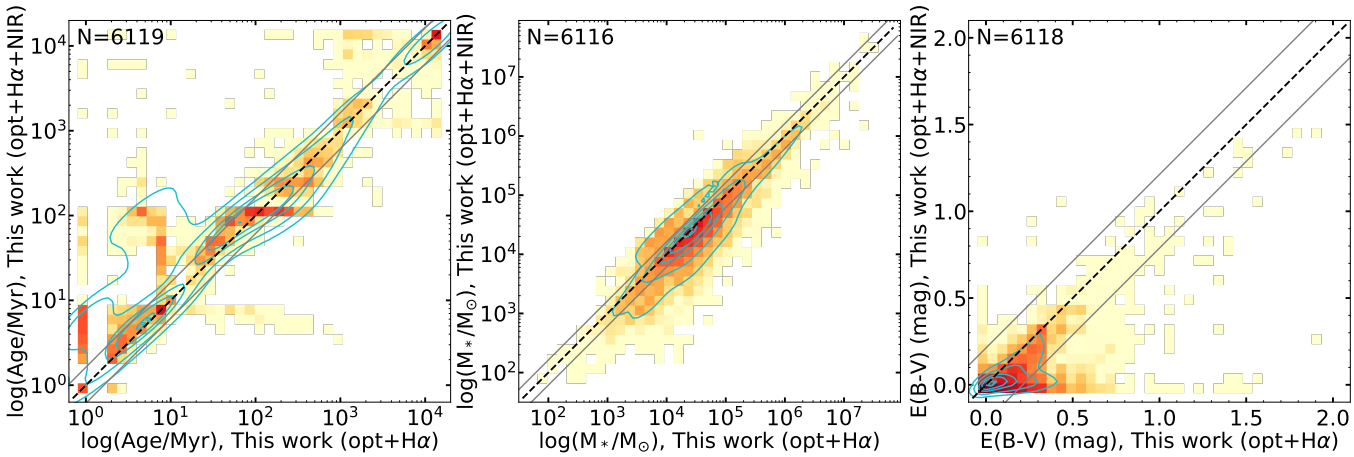

Figure 9. Comparison of HST-only vs. HST+NIRCam modeled results for age, mass, and $E(B-V)$. The data are plotted by number density of clusters, with contours representing density. Contours from outermost to innermost enclose 90%, 75%, 50%, 32%, 5%, and 1.5% of the total number of clusters.

4.2.1. Breaking the Age–Reddening Degeneracy between Reddened Young Clusters and Intermediate-age Clusters

The dominant feature in the left panel of Figure 9 is a knot of clusters above the 1:1 line, which have best-fit ages younger than 10 Myr when only HST photometry is used in the fitting procedure, but ages between 20 and 100 Myr when NIRCam measurements are included. Almost none of these clusters made the EW(Hα) cut of 80 Å, so they were fit with the general grid rather than the young, gas-rich grid. Of all clusters fit with an age $<$10 Myr with HST broadband + Hα, 680/2631 (or $\sim$25%) increase in age with NIRCam data to form the age–age offshoot "knot" in Figure 9. We divide these clusters into two groups that correspond to segments of this knot: one with larger discrepancies where HST-only age estimates are younger than 10 Myr but HST+NIRCam cluster ages are estimated to be 50 Myr or older ("extreme" age increases), and a second group where the HST+NIRCam age estimates are between 20 and 50 Myr ("moderate" age increase). We explore the nature and likely ages of these two subsamples below.

In Figure 10, we see the distribution of EW(Hα) for all clusters that changed from $\leqslant$10 to $>$20 Myr with the addition of NIRCam filters. We can see that the vast majority of these clusters have Hα equivalent widths well below the 80 Å threshold, centered around EW(Hα) = 0, which aligns with a population of exposed clusters. We manually investigated the clusters in the small bump between 50 and 80 Å, as these clusters would be the most likely to be edge cases where the EW(Hα) threshold failed. Individual examination confirmed that their moderate Hα was generally diffuse and unlikely to originate from the clusters themselves, and the general grid fit is most appropriate for them. From inspecting the images, we can also say that clusters in the age–age knot are generally not located in star-forming regions, and do not have blue SEDs consistent with young and exposed clusters. The small number of clusters that do have moderate Hα EWs show diffuse emission that is consistent with older clusters superposed on star-forming regions.

The top and bottom panels in Figure 11 show two examples of clusters that make up this age–age knot, and their respective modeled parameters with and without NIRCam. We can see that the HST broadband + Hα fit predicts higher reddening with strong near-infrared dust emission despite their total lack of Hα nebular line emission, and that when we include

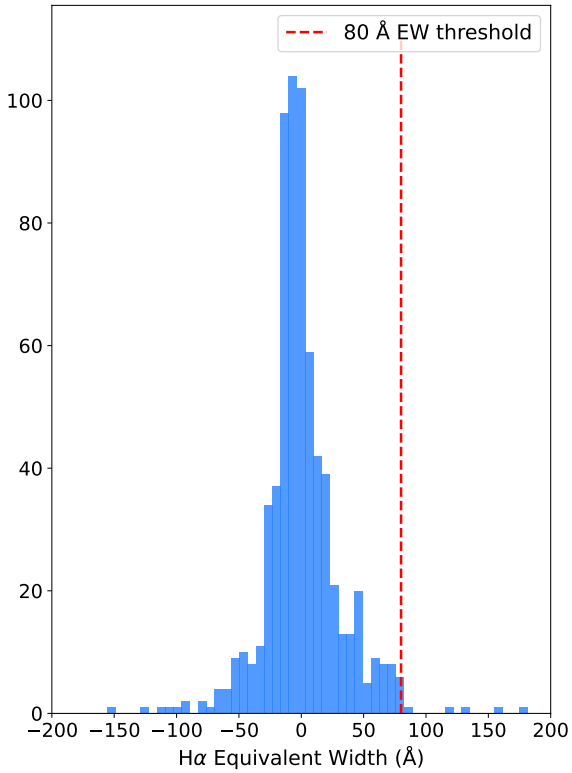

Figure 10. Histogram of the EW(Hα) distribution of all clusters that increased from an age $<$10 Myr to an age $>$20 Myr with the addition of NIRCam.

NIRCam, the near-infrared is constrained to the stellar continuum. The simultaneous presence of a red optical slope and a blue NIR slope, eliminates the possibility that these clusters could be young and reddened: if they were truly $<$10 Myr, the clusters would be capable of heating dust into the NIR regime, and the HST-modeled reddening would be accompanied by both NIR dust emission, and likely Hα emission. Instead, their lack of NIR emission above the stellar continuum means that their red optical slopes are much more likely due to the clusters' intermediate ages.

In Figure 12, we show the $U-B$ versus $V-I$ colors of clusters with the most extreme discrepant ages in the top panel and more moderately discrepant age estimates in the bottom panel. Perhaps not surprisingly, these clusters fall in a region

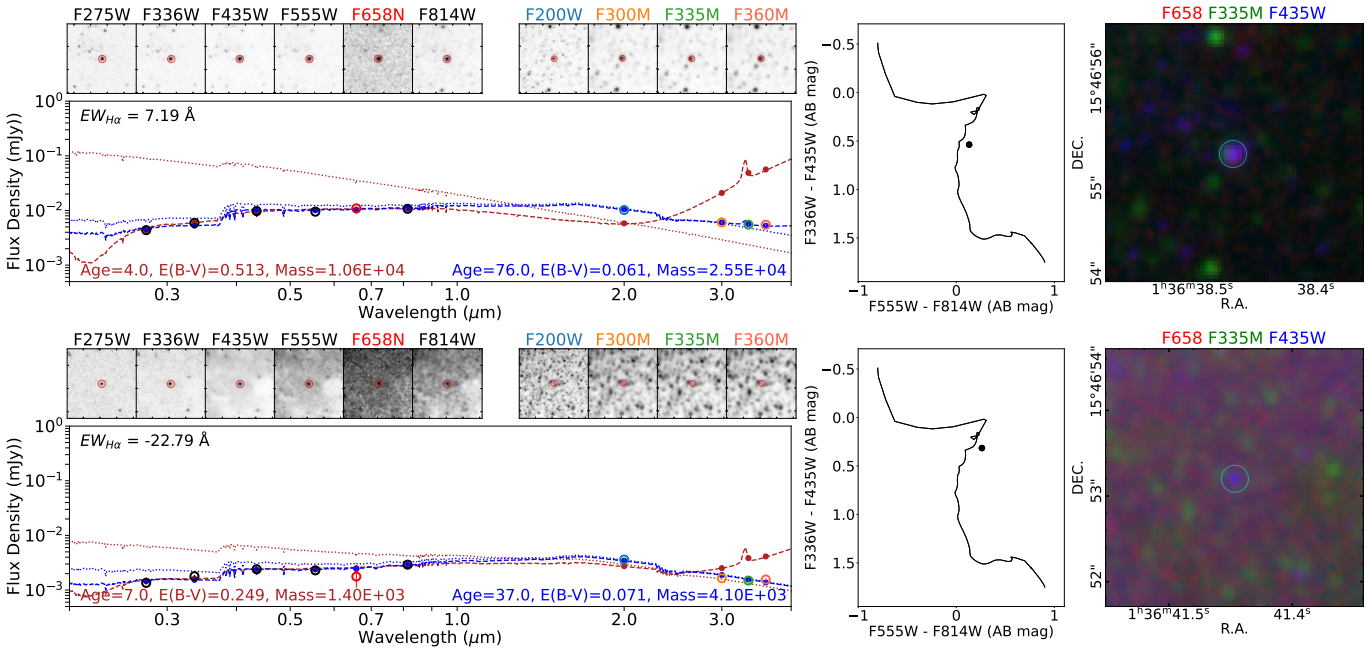

Figure 11. Top panels: example of a cluster with an "extreme" age increase to >50 Myr with the addition of NIRCam. HST broadband + Hα modeled parameters and SED are shown in red, HST + NIRCam modeled parameters and SED are shown in blue. Bottom panels: example of a cluster with a moderate age increase to 20–50 Myr. Dashed lines are the total modeled flux, and dotted lines are the modeled stellar continuum.

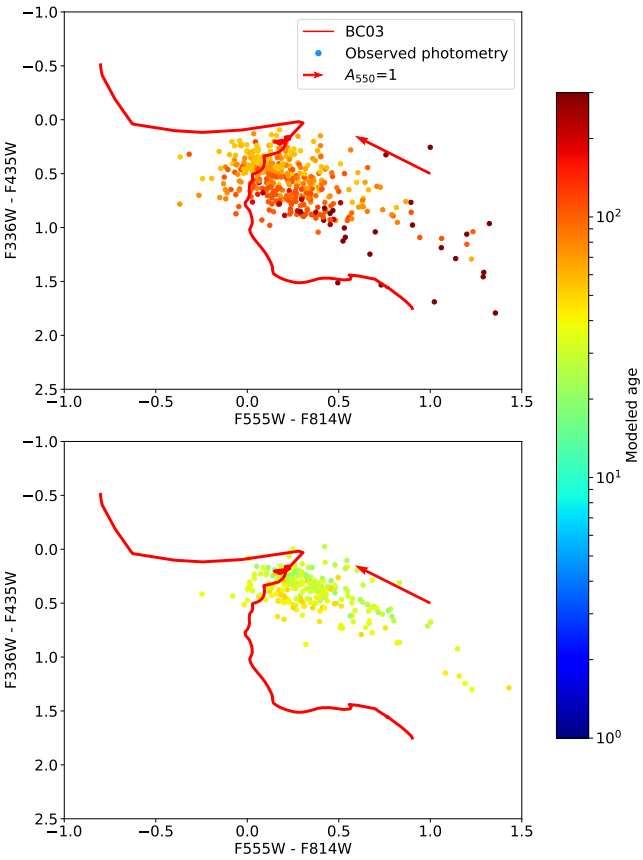

Figure 12. The $U-B$ vs. $V-I$ colors of clusters that have discrepant best-fit age estimates between the HST-only (<10 Myr) and HST+NIRCam (>20 Myr) fits, with BC03 stellar track shown. The top panel shows more extreme outliers where HST+NIRCam finds ages >50 Myr, and the bottom panel shows clusters with best-fit HST + NIRCam ages of 20–50 Myr.

of the color–color diagram where multiple combinations of age and reddening can provide a good fit to the SED. HST +NIRCam modeling finds that older ages and lower reddening fits better describe the SEDs for these clusters. We conclude that while the inclusion of HST-Hα data in SED modeling does effectively identify clusters that are truly young and gas-rich rather than intermediate-age and exposed, it is not sufficient on its own to break the reverse direction of age–reddening degeneracy. Including NIR filters in SED modeling leads to significantly improved age estimates for clusters with optical colors that are difficult to accurately model with optical-only data, demonstrating that the inclusion of NIR filters effectively breaks the degeneracy between the young-dusty and exposed-intermediate solutions for clusters that are truly intermediate-age and exposed.

4.2.2. How NIRCam Influences Changes in Age–Mass–Reddening Space: Resolved Degeneracies

Changes in the modeled age–mass space illustrate multiple different ways the addition of NIRCam affects modeled results and our interpretation of them: (1) Clusters with age–reddening degeneracy issues that are resolved with NIRCam, and (2) Clusters that illustrate the weaknesses of the BC03 stellar model in the first 10 Myr. Figure 13 shows both the changes for all clusters in a single galaxy overall (NGC 628c), and four examples of these two kinds of age–mass shifts.

The first category of age–mass shifts is that of clusters moving from a young <10 Myr solution, to an older solution. These clusters either stay the same or increase in mass. Because NIRCam reveals that these clusters do not have NIR dust emission, and instead show only the stellar continuum in the NIR, we can be confident that their increased ages and same or increased masses better reflect their physical

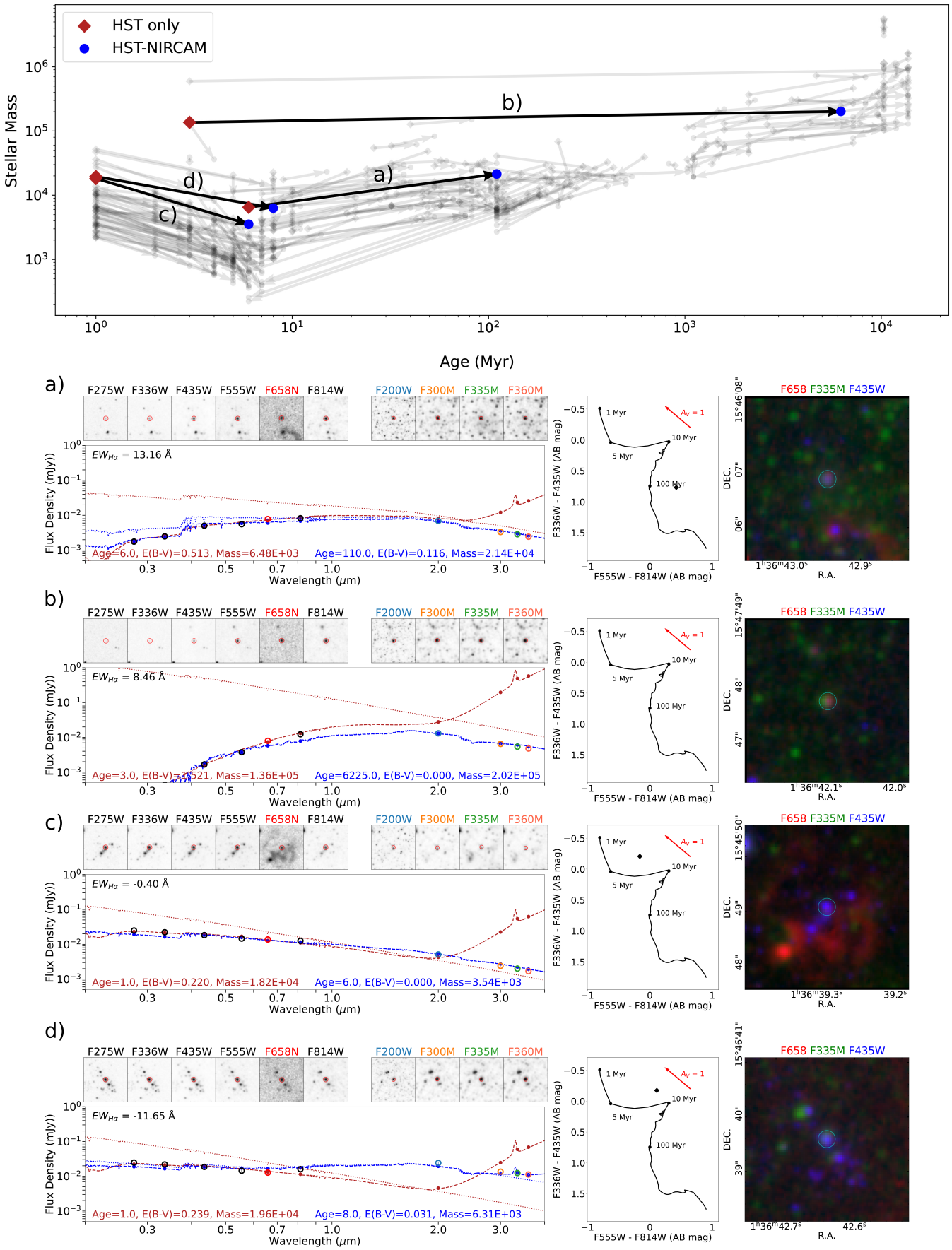

Figure 13. Top panels: age vs. mass of all clusters in NGC 628c (gray) with clusters exemplifying various types of age–mass changes highlighted. Bottom panels: the SEDs, color–color diagrams, and color images of the four clusters highlighted in the top panel. The HST-only results are shown in red, and the HST+NIRCam results are shown in blue.

properties. Cluster (A) in Figure 13 is an example of a cluster in the same population we described in Section 4.2.1. These clusters increase in modeled mass with the addition of NIRCam because their HST+NIRCam modeled age is old enough that we would not expect very bright young stars to be present, necessitating a larger stellar population to achieve the cluster's brightness. Cluster (B) exemplifies a cluster that, despite not having Hα emission, was still found to have a young and reddened solution with near-ultraviolet-optical filters. It is found to have an OGC age, reddening, and mass when NIRCam is added.

A handful of clusters like Cluster (B) are found in every galaxy. Although they are few in number, it is extremely important that we accurately model the ages and masses of the most-massive clusters, and with only HST filters, it would appear that nearby spiral galaxies contain a small population of extremely massive young clusters. The possibility of this population is especially interesting for those studying the formation and evolution of globular clusters, who are seeking to understand whether GC-like clusters are able to form in the present day or at high metallicities. When we add NIRCam filters and constrain the NIR, it is clear that many seemingly very-high-mass young clusters are actually old/globular clusters.

4.2.3. How NIRCam Influences Changes in Age–Mass–Reddening Space: Modeling Young Clusters

The second category of age–mass–reddening shifts is composed of clusters that are located above the 5–10 Myr portion of the BC03 stellar track in $U-B$ versus $V-I$ color–color space, redward/to the right of the 1–5 Myr portion of the track (henceforth referred to as the "basket" of the BC03 model) and relatively far from the 1 Myr start of the track. Examination of this category of clusters illustrate flaws in the adopted BC03 stellar models that reveal the uncertainty in cluster ages in the 1–10 Myr age range. Clusters (C) and (D) in Figure 13 both exemplify this uncertainty. Both move from 1 Myr and higher mass with HST filters, to an older, lower-mass solution when NIRCam is added. Both are located above the 5–10 Myr section of the BC03 stellar model. This means they have two options for solutions, given our chosen stellar continuum model: a 1–3 Myr solution with more reddening, and a 5–10 Myr solution with no reddening. The latter solution involves a much larger χ^2 than the former solution. When NIRCam information is introduced, revealing that the NIR SED is not compatible with a radiation field ($U = 10^6$) capable of heating dust into the NIR (B. T. Draine et al. 2007), a 1–3 Myr high-reddening solution would result in even larger χ^2 than the 5–10 Myr solution, and an age directly below the cluster's position in $U-B$ versus $V-I$ space is assigned, with a lower mass. As we can see in Figure 6, one of the major areas where clusters are located below the luminosity limit in age–mass space is right around the 5–10 Myr age range, and we can see that most of these clusters modeled as being low mass and 5–10 Myr with HST+NIRCam have moved from younger/more massive solutions with HST.

Cluster (C) has a mildly blue optical slope, and an NIR slope aligning with a pure stellar continuum. This cluster cannot have a large amount of reddening and simultaneously have massive blue stars. It may be that the cluster is very young but due to stochastic mass sampling, OB stars are underrepresented, or it may truly be a slightly older cluster whose most-massive stars have started to evolve, leading to a milder blue slope. Cluster (D) exhibits a flat optical slope, an elevated 2 μm flux, and an observed NIR slope that is flatter than the intrinsic stellar continuum. The presence of supergiant (<50 Myr) and asymptotic giant branch (AGB; 100 Myr–1 Gyr) stars causes significant elevation of the flux of a stellar population at NIR wavelengths (M. Mouhcine & A. Lançon 2002), and this cluster likely already contains evolved stars that cause its 2 μm flux to become elevated and are creating new dust. Given the cluster's location relatively high in the color–color diagram and overall SED shape, the presence of one or more red supergiant stars is the most likely option, as they appear between ~6 and 15 Myr. Red supergiant (RSG) stars are extremely dominant in the NIR: generally when studying resolved stellar populations, stars ~4 mag brighter in the K band than any other star are considered RSGs (B. Davies et al. 2007), and spectra of RSG stars peak at various points in the NIR redward of the F814W filter depending on temperature (J. T. Rayner et al. 2009). With no signs of natal gas and dust, which would be indicated by the presence of Hα or PAH emission, the HST+NIRCam fitted age of 8 Myr is much more likely than the HST-modeled age of 1 Myr.

The youngest clusters form a clump that is above the 5–10 Myr horizontal part of the BC03 stellar track, and which is also not close to the 1 Myr tip of the track. This "young cluster locus," described and discussed in D. Maschmann et al. (2024b) and shown in Figures 6 and 8 of that work, is composed primarily of Class 2 clusters (concentrated, single-peaked but asymmetric) that are very likely younger than 10 Myr. This inconsistency between the actual distribution of clusters in $U-B$ versus $V-I$ color–color space and the BC03 stellar track has been discussed in D. Maschmann et al. (2024b), S. Deger et al. (2022), and J. A. Turner et al. (2021), and it has been shown that the shape of the BC03 track in the first 10 Myr is not consistent with actual stellar populations. However, in these previous modeling works, it has been difficult to definitively place restrictions on the dust affecting individual clusters in this range and determine how clusters' intrinsic colors evolve at the youngest ages. The addition of NIRCam helps us place much more confident restriction on the reddening of clusters in the young cluster locus.

Despite the limitations of performing small-aperture photometry in the NIR, where we observe a huge range of gas and dust extendedness from very concentrated to very complex and extended (see Figure 1 and Section 5.2 for examples of this diversity), there is an obvious difference in the SED of a cluster that has hot dust present, and one that does not. This basic difference, clearly shown in the HST-only (red) and HST +NIRCam (blue) fits in clusters (C) and (D) of Figure 13, provides us with a valuable tool in testing stellar models at young ages. A lack of hot dust emission in a cluster rules out all solutions that are simultaneously rich in OB stars and reddened, and is extremely helpful in disentangling age–reddening degeneracy between 1 and 3 Myr clusters and other clusters that are less than 10 Myr. These clusters help us understand the uncertainties in the modeled ages of young clusters in our sample that do not have Hα above the EW threshold.

Hα emission is a strong indicator of a cluster's young age, as is NIR dust emission, and so fits of clusters that exhibit EW(Hα) above the threshold and have NIR dust emission

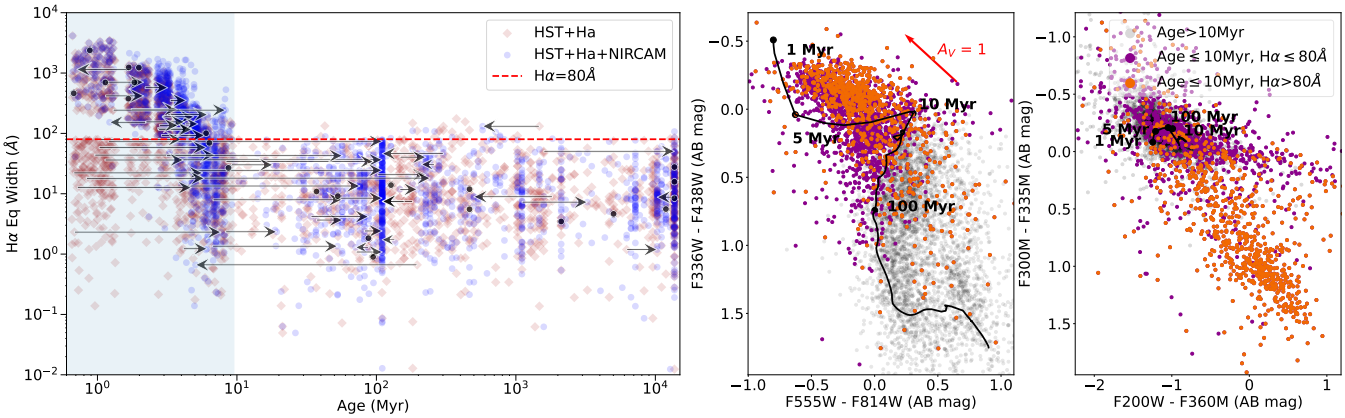

Figure 14. Left panel: all clusters in age–Hα EW space. A random offset of [−0.35, 0.35] has been added to all ages, to better visualize cluster density in the youngest age bins. Red: cluster ages fitted with HST broadband+Hα. Blue: cluster ages fitted with all HST+NIRCam filters. Black arrows and points: movement in age–space of 200 randomly selected clusters from our sample of 6129 clusters. Points represent clusters that did not change in age with the addition of NIRCam. Center panel: $U-B$ vs. $V-I$ plot of clusters modeled as <10 Myr with HST+NIRCam, corresponding to blue points falling within the shaded region of the age–Hα EW plot. Purple points are clusters modeled as ⩽10 Myr with Hα EW < 80 Å, orange points are clusters modeled as >10 Myr with Hα EW < 80 Å, and light-gray points are all other clusters. Right panel: F300M − F335M − F200W − F360M color–color plot with the same cluster groups as center panel.

often yield ages of 1–3 Myr. Out of our entire population of <10 Myr clusters, we view these gas- and dust-rich clusters with the smallest uncertainties for ages, masses, and reddenings. However, young exposed clusters without Hα emission above the EW threshold generally lack the influence of Hα and NIR dust emission that drive SED fits to young solutions, and so are much more likely to be assigned to the 4–10 Myr age range unless they exhibit very steeply blue NUV-optical-NIR SED slopes. This leaves young clusters without Hα emission with mildly blue or "flat" SED slopes as the population with the greatest model-dependent age uncertainty. Because it is clear that the $U-B$ versus $V-I$ shape of the BC03 stellar track does not conform well to actual cluster distributions in the first 10 Myr, we only go so far as to claim that clusters without detected Hα and assigned ages of 5–10 Myr are relatively gas- and dust-free and likely younger than 10 Myr.

In Figure 14, we can see that clusters' Hα EW is highly predictive of an HST+NIRCam modeled age ⩽10 Myr, and that as Hα EW decreases, clusters are generally modeled with increasing age in the first 10 Myr. In the center and right panels, all clusters modeled as being ⩽10 Myr with HST +NIRCam (blue circles in shaded region of left panel) are shown, in purple if they do not meet the Hα EW, and in orange if they surpass the threshold. We can see that while they are highly overlapping in $U-B$ versus $V-I$ color space, in NIRCam (F300M − F335M − F200W − F360M) color space, the two populations are very separated. The F200W − F360M axis separates clusters with continuum hot dust from those without, while the F300M − F335M axis separates clusters with and without 3.3 μm PAH emission. While there is a population-level separation between ⩽10 Myr clusters above and below the 80 Å threshold, there is still overlap. This overlap illustrates both how Hα and NIR dust emission do not map perfectly on each other, and also that clusters with strong Hα EW can have a large range of dust emission strengths.

Our ability to interpret young cluster subpopulations in color–color space is also informed by stellar evolution. When the most-massive stars start to evolve, they impact a cluster by flattening its NIR SED as NIR-bright evolved stars start to dominate the cluster and also generate new hot dust. This can be seen in the right-hand F300M − F335M − F200W − F360M color–color plot, in the shallowly sloped, mostly horizontal band of purple points (exposed young clusters) with F300M − F335M ∼ 0. While clusters with very bright F200W compared to F360M (left side) generally have slopes aligning with a hot massive stellar continuum, those farther to the right, with more moderate differences between F200W and F360M, often exhibit these flatter SEDs. SED modeling is able to model these features of clusters' SEDs that are difficult to capture even with the aid of multiple four-filter color–color diagrams. With all 10 bands, it is quite apparent when clusters' NIR behavior is due to a young, blue stellar population, or the effects of NIR-bright evolved stars.

NIRCam's constraint on the possible amount of reddening a cluster experiences, reveals that the BC03 stellar continuum model does not reflect well the actual observations of star clusters in the first 10 Myr. However, combined with HST filters, it does provide us with enough information to construct stellar evolution tracks that do align with actual stellar populations.

4.2.4. Old/Globular Clusters

While including NIRCam photometry improves the accuracy of age estimates for young and intermediate-age clusters, it does not provide significant advantages for identifying or modeling ancient globular clusters. We used a test sample of manually identified OGCs, which were categorized as such with two independent methods (M. Floyd et al. 2024; D. A. Thilker et al. 2025), and examined every possible four-filter color combination of our 10 available filters to see if any combination performed better than the optical-only $U-B$ versus $V-I$ (and B versus $V-I$) criteria used by D. A. Thilker et al. (2025). We found that $U-B$ versus $V-I$ color along with B versus $V-I$ color–magnitude continued to show the greatest separation of OGCs from other cluster subpopulations. Since the shape of the NIR stellar continuum evolves slowly at older population ages, this result is not surprising.

We find that modeling OGCs with the general grid results in ages >400 Myr for >95% of clusters mutually identified by D. A. Thilker et al. (2025) and M. Floyd et al. (2024). While this is not a reasonable age for OGCs, it is noteworthy that very few clusters designated as general or YGR clusters

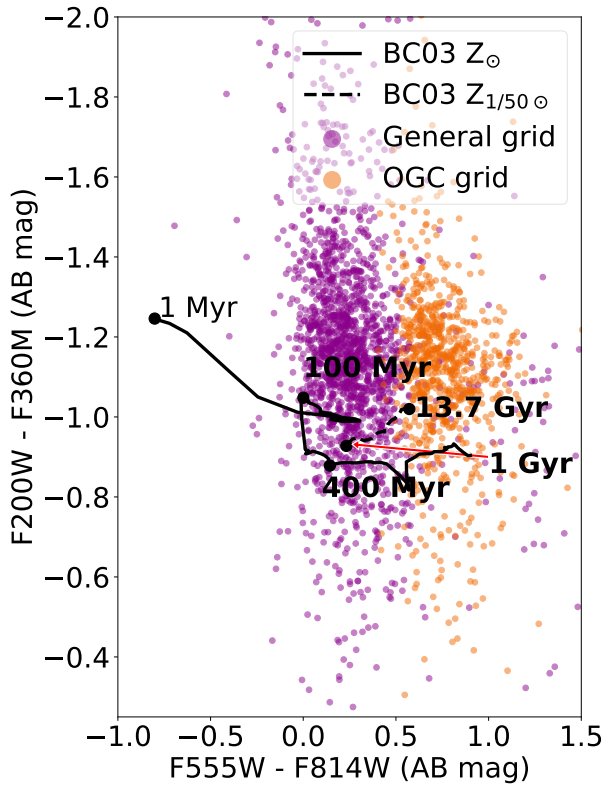

Figure 15. Optical $V-I$ vs. NIR 2.0–3.6 μm color–color plot showing general grid-selected clusters vs. OGC grid-selected clusters (points) and the BC03 solar and 1/50th solar metallicity tracks. The two populations have completely overlapping NIR colors, but distinct optical colors.

are modeled or expected to exist at ages this old. The combination of 10 NUR-optical-NIR filters is identifying elements of SED shapes that bias toward old ages in clusters identified as OGCs. We also find that dropping even a single filter leads to a lower percentage of confirmed OGCs being modeled with old ages, suggesting that with the combination of all 10 filters, we may be able to even more accurately select OGCs than when using any combination of four filters. We manually verified that these modeled-with-OGC-age clusters, to the best of our ability to determine, are indeed possible OGCs that are slightly outside the canonical $U-B$ versus $V-I$ and B versus $V-I$ zones we adopted for OGCs. We chose not to constrain age for our young and general grids to allow for the possibility that clusters like these are best fit by old, low-reddening solutions. OGCs have a very strong "turnover" between the optical and NIR in both their modeled stellar continuum and observations, as illustrated in Figure 15. OGCs have a redder NUV-optical SED than younger, higher-metallicity clusters in the general grid, due to their lack of younger bluer stars, while the NIR is very similar for the two populations. In Figure 15, we can see that the intermediate ages from 100–400 Myr in the BC03 track, where most solar-metallicity older clusters fall, are to the left of the entirety of the 1–13.7 Gyr 1/50th solar track.

4.3. Comparison with Other Age-dating Results

4.3.1. Comparison with D. A. Thilker et al. (2025)

Recently, D. A. Thilker et al. (2025) used the same five broadband filters plus HST-Hα observations to estimate the age, reddening, and mass of clusters in PHANGS galaxies. We have adopted their OGC identification method after validating it with NIRCam data, and now we compare our method of identifying YGR clusters, with their young nebular object (YNO) selection method. YNO clusters must overlap with Hα segment maps (a cluster must be centered within an Hα segment, or have the Hα segment maximum fall within the cluster's 4 pixel aperture, or an Hα segment must cover >50% of the 4 pixel aperture), and also have an HST-Hα background-subtracted surface brightness between 1.1 and 20×10^{-16} erg s^{-1} cm^{-2} arcsec^{-2}, where the threshold is determined to be the 5th percentile of the HST surface brightness in the subset of clusters that have both ground-based and HST detections of Hα. D. A. Thilker et al. (2025) implemented both ground-based and HST-Hα measurements to decide whether a cluster should be modeled by their YNO branch, and found that HST's higher resolution was more accurate at identifying clusters with associated nebular emission than ground-based Hα data (96% versus 99% when 100 randomly selected YNO clusters in a sample were examined individually). Because HST-Hα is only available for half of the full PHANGS sample, one key goal of that work is to assess how well one can use ground-based Hα imaging with HST broadband filters to age-date star clusters. With the lower resolution of ground-based Hα imaging, clusters that are actually exposed have lower-resolution Hα emission that is bright enough to fulfill the criteria used in D. A. Thilker et al. (2025) and be incorrectly selected for the YNO grid.

The aim of the YNO classification is slightly different than our YGR classification, which is reflected in the nebular model parameters selected. All YNO clusters are modeled with an age grid of 1–5 Myr, and $f_{\rm esc}=0.5$. This means that the SEDs of YNO clusters should generally be significantly influenced by nebular emission, and should not include clusters that are mostly exposed with some Hα emission. In other words, clusters in the centers of extended H II regions that have weaker Hα emission would ideally not be included. This is in contrast to our approach, which identifies all young clusters whose SEDs are even somewhat influenced by nebular emission, which is reflected by our choice not to restrict age, and to allow $f_{\rm esc}$ from 0.5–1.0. We will refer to the results of the D. A. Thilker et al. (2025) method as "SEDfix" ages, reddenings, and masses, and examine how the YNO selection criteria affect derived cluster properties later in this section.

We compare the ages from our HST-only and HST +NIRCam fits with these SEDfix fits in the first column of Figure 16. In the top panel, we find good agreement for the majority of cluster ages, except for a small "spur" containing 325/6130 or 5.3% of the sample when comparing our HST +Hα fits with theirs. Whereas D. A. Thilker et al. (2025) found ages 20–100 Myr, our HST fits find ages younger than 10 Myr. This spur becomes negligible when NIRCam is added (first column, second row), and many of the clusters in this spur move up to form the age overdensity at 100 Myr.

When we compare our age results based on HST+NIRCam versus those from D. A. Thilker et al. (2025), we see similar trends as those described in Section 4.2, where overall, the majority of clusters have consistent age estimates, but there is a knot of clusters that appear to be older than 10 Myr when NIRCam data are included in the fitting procedure. We checked these clusters, and confirm they are similar to those discussed in the previous section. This knot is less dense than

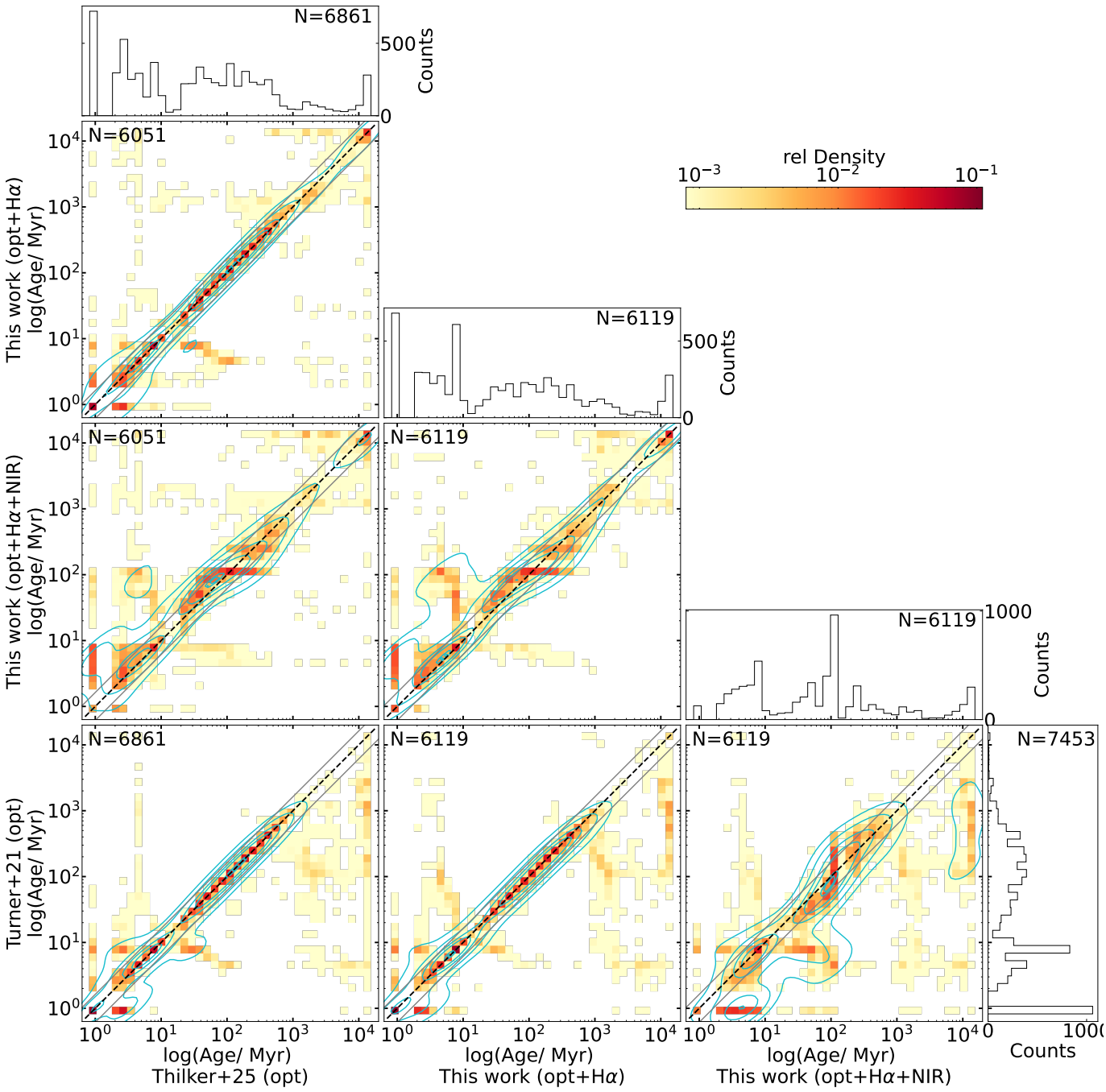

Figure 16. Age distribution comparison of the HST broadband + Hα and HST + NIRCam results of this work with age distributions of D. A. Thilker et al. (2025) and J. A. Turner et al. (2021).

the same knot in our comparison of our own HST versus HST +NIRCam results, which is an effect of the grid selection in the SEDfix YNO branch. Because clusters that are flagged for the YNO branch on the basis of their Hα surface brightness and their overlap with Hα segment maps are modeled with a restricted age range of 1–5 Myr, when comparing these two methods, the SEDfix age bin from 1–10 Myr contains both YNO clusters forced to 1–5 Myr, and clusters without Hα emission with no age restrictions. This means the 1–5 Myr age bin includes both YNO and general clusters, but the 5–10 Myr bin only contains general clusters. This has the effect of causing the knot of clusters that change age to be less defined and dense.

In Figure 17, we compare the reddening distributions of the cluster catalog derived via the same few methods. We can see that there is a distinct bifurcation of reddening when comparing HST+NIRCam-derived reddening with HST-only-derived reddening. Many clusters which were modeled with more reddening when only using HST filters, are modeled with little-to-no reddening when NIRCam filters are added. This illustrates the issue described in Section 4.2.3 where young clusters in the "basket" of the BC03 track can end up with likely-unrealistically low reddening and ages in the 5–10 Myr range.

In Figure 18 we compare mass estimates between our results and those of D. A. Thilker et al. (2025). In general, for low-

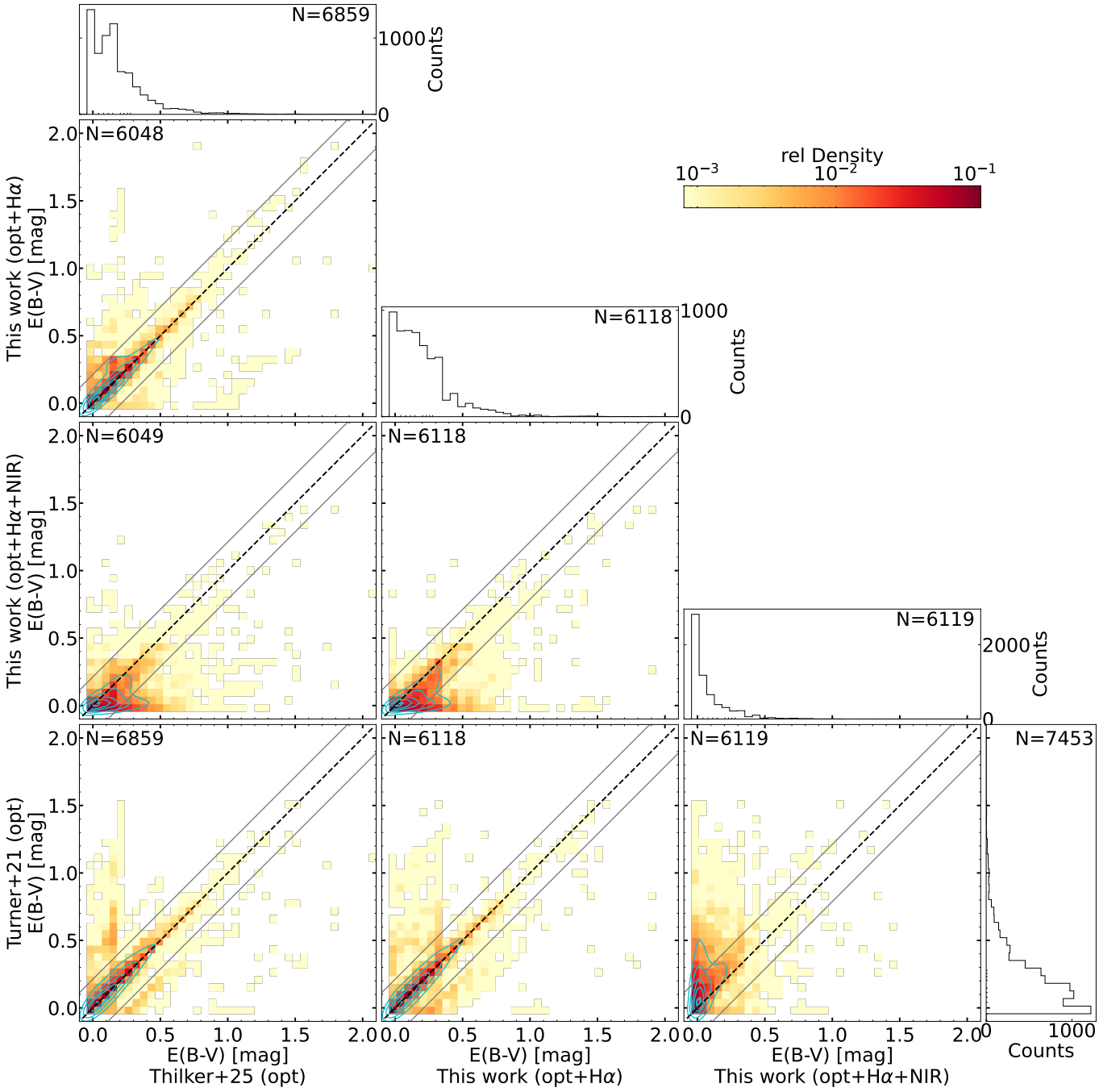

Figure 17. Reddening ($E(B-V)$) distribution comparison of the HST broadband + Hα and HST + NIRCam results of this work with age distributions of D. A. Thilker et al. (2025) and J. A. Turner et al. (2021).

mass clusters, our HST+NIRCam method finds lower masses than the SEDfix method, and higher masses for the high-mass clusters than does the SEDfix method, similarly to the comparison between our own method with and without NIRCam. The low-mass clusters where we model a lower mass than the SEDfix method are generally young clusters where SEDfix finds ages of 1–3 Myr with higher reddening, and our HST+NIRCam method finds ages of 6–10 Myr due to a lack of NIR dust emission, in parallel to the phenomenon we discussed in Section 4.2.2.

One of the main differences between the SEDfix method and the approach outlined in this this work is in the selection of clusters for the respective YNO or YGR grids. The SEDfix method flags more clusters overall than our EW(Hα) method. We examine how differences in the selection criteria used to identify reddened/gas-rich young clusters affect the quality of the resultant cluster selection. We have carefully examined the clusters selected for these grids in four galaxies: NGC 4321, NGC 628c, NGC 3351, and NGC 1672, and compiled our findings in Table 5.

We made a detailed investigation of the clusters in these four galaxies that were either exclusively flagged for the SEDfix YNO branch, or exclusively flagged by the method in this work for the YGR cluster grid. Because this investigation

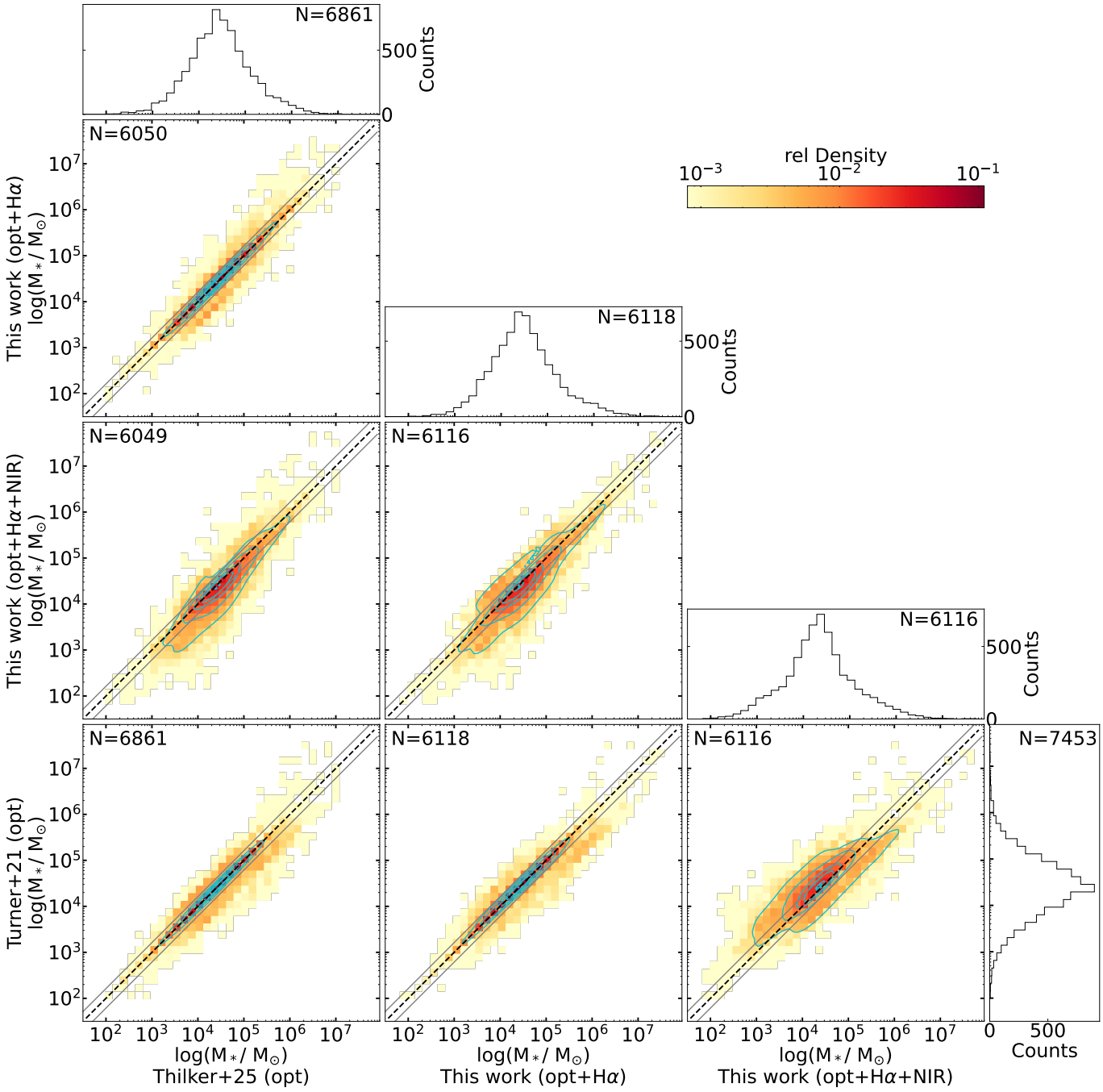

Figure 18. Mass distribution comparison of the HST broadband + Hα and HST + NIRCam results of this work with age distributions of D. A. Thilker et al. (2025) and J. A. Turner et al. (2021).

required careful examination of each cluster individually, we limited our investigation to these four galaxies rather than the entire sample of 16 galaxies. We utilized the diagnostic tools shown in Figure 1 to classify these mutually exclusive possible "young" clusters into the following five categories:

1. *Category A*. Clusters where the YGR grid is appropriate. These clusters have strong Hα flux and morphology that is obviously tied to the cluster and also show NIR (dust) emission.
2. *Category B*. Clusters that are clearly young, but do not have significant Hα and so are well-modeled with the general grid. These clusters have a blue optical and NIR SED. If they have Hα line emission above the continuum, it is weak.
3. *Category C*. Clusters that appear to be older than 1–10 Myr. These clusters may appear red in the optical, and may have Hα above the stellar continuum, but their SEDs turn over and decrease in brightness through the NIR. This "turnover" means that their red optical slopes cannot (primarily) be due to dust reddening, making them likely older clusters.
4. *Category D*. Clusters that have identical, or nearly identical, age, reddening and masses in YGR and general grids used in this work. These clusters are optically blue.

Table 5
Counts of Clusters Identified as Young and Requiring Nebular Emission with at Least One Method

Category	Overlapping N/A	This Work						D. A. Thilker et al. (2025)					
		A	B	C	D	E	Total	A	B	C	D	E	Total
NGC 4321	30	5	1	2	1	0	9	3	13	10	9	1	32
NGC 628c	37	0	0	0	0	0	0	4	7	17	4	0	31
NGC 3351	16	1	1	0	1	0	3	3	10	6	4	0	23
NGC 1672	64	1	0	0	0	0	1	3	8	34	8	1	54
Total	147	7	2	2	2	0	13	13	38	67	25	2	140

Note. "Overlapping": clusters were flagged by both this work and D. A. Thilker et al. (2025); "This Work": clusters were flagged only by their EW as outlined in Section 2.3, but not by D. A. Thilker et al. (2025); "D. A. Thilker et al. (2025)": clusters were only flagged by D. A. Thilker et al. (2025) but not flagged by their EW. Categories A–E are described in Section 4.3.1.

For the YGR grid fit, they have high f_{esc} values of 0.8–1.0 (an $f_{esc} = 1$ solution in the YGR grid will always be identical to the general grid solution). Identical solutions with and without nebular emission indicate that these clusters are exposed, are only minimally affected by nebular emission, and don't require it to find a reasonable fit. These clusters are appropriately fit by both the YGR and general grids.

5. *Category E.* Clusters where the aperture is contaminated with a very nearby neighbor, and it remains unclear what the "true" SED is. The most problematic contamination issues are when a cluster is older and relatively dim in the NIR, but a nearby young object with strong Hα and/or NIR dust emission is also within the aperture.

We closely examined each individual cluster that was either flagged as YGR (this work) or flagged as YNO with the SEDfix method but *not* flagged with both methods. Clusters that were flagged by both works as requiring nebular emission were inspected more generally, and we determined that these overlapping clusters were appropriately selected. We can interpret clusters flagged via just one method as follows: clusters in Category A can be viewed as having been "missed" by the other method. Clusters in Category D can be thought of as having been appropriately identified by each respective method and not "missed" by the other method. Clusters in Categories B and C can be considered "misclassified" by the method that assigned them to a young grid with nebular emission, and would be more appropriately modeled without nebular emission. Clusters in Category E are beyond either work's ability to accurately model due to contamination effects. Table 5 shows the breakdown of these YNO/YGC clusters that were flagged with only one method, as well as the number of clusters that both methods flagged (the "overlapping" category).

For all four galaxies, D. A. Thilker et al. (2025) classified approximately 2 times more clusters for their YNO grid than we classified for the YGR grid. Category B and C clusters, both evaluated as being most appropriately modeled without nebular emission, are the largest categories, with a combined 2.5 times more clusters than Categories A and D. Note that 13/140 clusters exclusively classified as YNOs by D. A. Thilker et al. (2025) were "missed" by our EW(Hα) approach.

The largest category of clusters exclusively classified as YNOs by D. A. Thilker et al. (2025) is category C, clusters evaluated to be older clusters when examined with NIRCam data. This population, composed of star clusters that in the optical could be either young, moderately reddened clusters or intermediate-age, low-reddening clusters is the same population as the one described in Section 4.2 and earlier in this section.

The YNO identification method, which generally is more inclusive than our EW(Hα) method, does identify some clusters that we miss, but also includes a large number of clusters whose intermediate-age identities are revealed with NIRCam. The SEDfix method correctly age-dates clusters in the young-intermediate-age degeneracy slightly more than when only HST broadband and Hα are used with our method, but the addition of NIRCam to NUV-optical bands is even more effective at breaking this degeneracy.

4.3.2. Comparison with SED Fits from Broadband-only HST Photometry

As described in Section 3, the PHANGS-HST SED fits from J. A. Turner et al. (2021) adopt a single set of priors with the BC03 stellar models, solar metallicity, and $E(B-V) = [0...1.5]$, and does not include nebular or dust emission.

The bottom row of Figure 16 and the corresponding histogram on the far right shows the age results of this approach. With no Hα included, and only solar metallicity models, we see a very large number of young, 1 Myr clusters, almost no 2–5 Myr clusters, and almost no OGCs. With optical broadband only, CIGALE finds best fits for a young, high-reddening solution for a very large proportion of clusters. Including a tracer of nebular emission both as a selection criterion and directly in the SED fitting procedure significantly improves age results, particularly showing a much more even age distribution of young clusters, with no overdensity of 1 Myr clusters. We can see this in the bottom-right panel of Figure 16, where we see that the 1 Myr spike in J. A. Turner et al. (2021) is much reduced in HST+NIRCam, and there are similar numbers of 1, 2, and 3 Myr clusters in our HST +NIRCam results.

Without using multiple sets of priors for solar and subsolar metallicity, ~80% of old globular clusters are incorrectly age-dated to be younger than 1 Gyr with moderate to high reddening. With only solar-metallicity-models, these OGCs are redistributed from ages 1–13 Gyr, to multiple younger ages: very young, very high-reddening solutions, and more intermediate ages with moderate reddening, with the majority falling into the latter category. We see in the bottom row of Figure 16 that for all fits that incorporate multiple sets of priors and place age and/or reddening restrictions on the OGC priors, that many clusters have been redistributed from intermediate ages of ~100 Myr to 1 Gyr to older, more appropriate ages of >10 Gyr.

5. Modeling Dust Emission and the Smallest PAHs

A low $q_{\rm PAH}$ mass fraction aligns best with the strength of the 3.3 μm PAH feature for all HST-identified YGR clusters, even for the youngest and most gas- and dust-rich clusters. The high number of young, gas- and dust-rich clusters with strong, concentrated Hα within a 4 pixel aperture, and rings or partial shells of 3.3 μm emission outside the cluster aperture, indicates the need for a more complex treatment of dust to account for dynamical factors such as grain destruction and stellar winds when incorporating the 2–3.6 μm range into star cluster SED fitting.

5.1. H II Regions and the 3.3 μm PAH Feature

The 3.3 μm PAH feature is covered by the F335M band for local galaxies and somewhat contaminates the F360M band along with the 3.4 μm aliphatic feature and the 3.47 μm "plateau" feature (K. M. Sandstrom et al. 2023). It is the only PAH feature we observe in the NIR, and provides constraints on the abundance of the smallest PAHs. Small PAHs have low heat capacities, and thus, they can easily be heated to high peak temperatures after absorbing UV photons (D. Baron et al. 2024; B. Gregg et al. 2024; A. Pedrini et al. 2024). Along with Hα, the presence of the 3.3 μm feature is a good indicator of a cluster's young age.

Dynamical and morphological mapping of clusters with a 3.3 μm PAH feature indicates that these PAHs disappear from a cluster's immediate environment within a few million years (B. C. Whitmore et al. 2025), more quickly than Hα emission. This is compatible with our understanding of PDRs in the Milky Way, where we see H II regions surrounded by 3.3 μm shells (R. Chown et al. 2024). Whether the smallest PAHs are destroyed or blown away from clusters forming H II regions, we expect all but the youngest and most embedded clusters to exhibit Hα emission closest to YGR clusters, with hot dust and small PAHs emitting farther away from the clusters.

Infrared observations of Milky Way H II regions and their associated PDRs dating back to the Infrared Space Observatory era have shown that ionized gas, molecular gas, and dust emission are not necessarily cospatial (e.g., D. Cesarsky et al. 1996). Studies of H II regions in the Milky Way, LMC, and SMC (e.g., K. M. Sandstrom et al. 2012; J. Chastenet et al. 2019) have demonstrated that the overall PAH fraction $q_{\rm PAH}$ is observed to be lower in H II regions and PDRs than in non-star-forming regions. O. V. Egorov et al. (2023) and J. Sutter et al. (2024) also found that the PAH fraction steeply decreases in H II regions.

The 3.3 μm feature has been relatively under-observed prior to JWST coming online compared to other PAH features. The AKARI InfraRed Camera (pixel size = 1.″46) and ISO ISOCAM (pixel size = 1.″5–12″) both covered the 3.3 μm feature, but there has been much less study of this feature than of longer-wavelength PAH features, which were extensively observed by ISO and Spitzer.

Recent works utilizing JWST NIRCam data have found that the 3.3 μm feature disappears from very young environments even more rapidly than larger PAH features: Figure 3 of D. A. Dale et al. (2023) showed that HST-selected star clusters align best with a PAH size distribution favoring large PAHs, with almost no clusters in the PHANGS-HST sample having high abundances of small PAHs relative to larger ones, and R. Chown et al. (2024) found that the atomic region of the Orion Bar PDR has a 40% lower 3.3 μm/11.3 μm ratio than within its H_2 dissociation front.

5.2. Dust Characteristics of YGR Clusters with the Strongest Hα Emission

Clusters in our catalog with the strongest Hα equivalent widths (EW > 150 Å and especially EW > 1000 Å) display a wide variety of gas and dust morphologies, from tightly concentrated and completely within a 4 pixel aperture, to extended or complex gas and dust morphologies that are seen on a scale much larger than our aperture size. Gas and hot dust emission is sometimes symmetric but more often is asymmetric, as would be expected as clusters blow out their gas and dust within or adjacent to molecular clouds with nonuniform densities. Figure 19 shows a sample of 10 clusters with strong Hα emission in NGC 628c representing the range of gas and dust morphologies of YGR clusters. We can see that while some clusters have very concentrated morphologies ((a) and (b)), others have clearly started forming bubbles ((c), (d), and (e)) and others are found on the edges of much larger star-forming complexes and are unlikely to be the primary contributors to the excitation of gas and dust in their immediate vicinity (clusters (f) and (j)). Others fall somewhere in between ((h) and (i)), with cases of contamination (j) also being present. Concentrated and symmetric clusters are few, and clusters with highly asymmetric gas and dust emission morphologies are the majority. While some H II regions show obvious stellar populations other than the clusters we are modeling ((f) and (g)), many H II bubbles and shells do not have populations of blue stars at their centers, indicating that the clusters in question may have formed these H II regions through a "blister" model, where the H II region runs into denser material in one direction but not another as they expand. Clusters (c) and (d) are particularly likely to be on the edges of dusty regions, as we can see that they show 3.3 μm emission only on one side of their respective Hα bubbles.

We find that even the most concentrated clusters in our catalog, like cluster (a) in Figure 19, show relatively low 3.3 μm PAH emission. This is apparent in Figure 3 from an SED standpoint, but is even more clear when we look at the 3–3.3 μm color specifically. Figure 20 shows the F300M – F335M modeled flux for several ages and reddening values and their corresponding $q_{\rm PAH}$ values at the left, and the observed F300M – F335M colors of YGR clusters in this work (blue), as well as clusters identified via their F300M – F335M excess, rather than with the HST F555W filter, by J. Rodriguez et al. (2023) for reference (pink and mint green). We can first see that YGR clusters exhibit a bimodal distribution of F300M – F335M colors, with peaks at 0 and 1 mag of difference. The first peak at 0 corresponds with clusters that have strong Hα but are mostly exposed. These clusters are characterized by blue, stellar continuum-dominated SEDs, and are generally within larger H II regions, and it's at least possible that they could have $A_V \sim 0.01$. The second peak, at 1, is composed of clusters with strong Hα that also have hot dust emission. We can see by the difference in the modeled PAH feature size between $A_V = 0.01$ and $A_V = 0.1$ that the size of the 3.3 μm feature rapidly increases with a small increase in A_V. It is unrealistic that clusters with both strong Hα emission and clear small PAH emission would have an $A_V < 0.1$, and thus, the clusters creating the peak at 1 most realistically align with very low $q_{\rm PAH}$ fractions. From a physical standpoint,

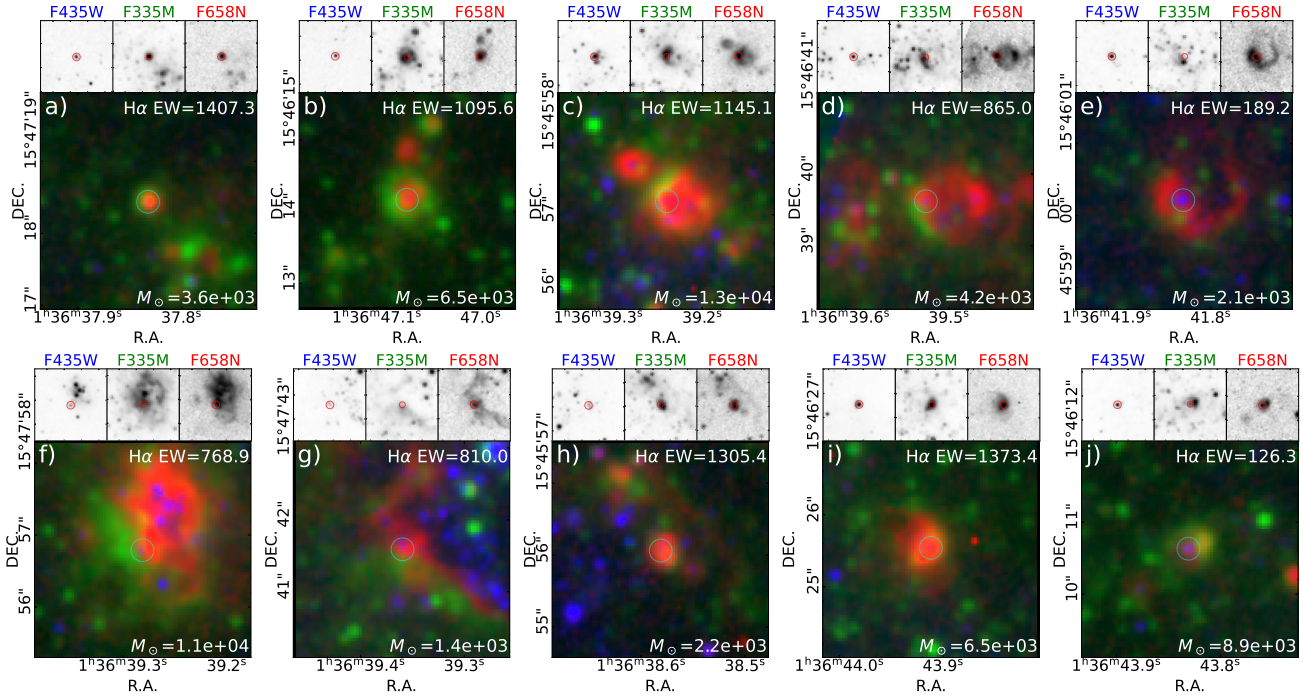

Figure 19. A sample of young clusters in NGC 628c with complex gas and dust morphology, encapsulating the wide range of morphological features we see. All filters and composite images have an asinh stretch applied. Some clusters ((a) and (b)) have tightly concentrated or concentric Hα emission and a high likelihood of being the primary source of ionizing photons, while others are on the edges of H II bubbles ((c), (d), and (e)). Clusters also fall at the edges of larger H II complexes ((f) and (g)), where it is unclear how much the clusters contribute to the overall energy balance of large complexes. Finally, it is sometimes unclear what the exact relationship between a cluster and surrounding Hα and hot gas is ((h), (i), and (j)).

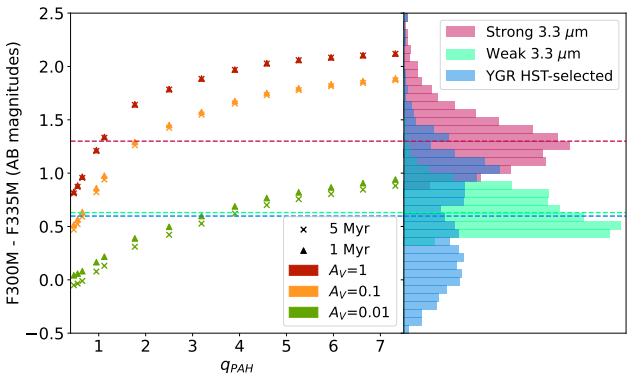

Figure 20. Modeled F300M − F335M color for $q_{\rm PAH} = [0.47...7.32]$ with BC03 stellar model and B. T. Draine et al. (2014) dust emission model (left) and normalized distribution of observed F300M – F335M colors of PHANGS-HST catalog clusters identified as YGR clusters (blue), and new embedded sources identified by J. Rodriguez et al. (2023). These were selected for their F335M excess (pink and mint green). $A_V = [0.01,0.1,1]$ are shown. Higher A_V values do not significantly change from $A_V = 1$.

YGR clusters with strong Hα emission but no significant hot dust emission (clusters in the peak centered at 0) are also unlikely to have high $q_{\rm PAH}$ fractions. As clusters and associations create H II regions, their intense radiation fields destroy PAHs. Thus, although the YGR clusters at the centers of H II regions may have very low A_V values, they are just as unlikely to have high $q_{\rm PAH}$ fractions as dustier YGR clusters. Given our understanding of PDR and H II region formation, and the restrictions this places on our interpretation of Hα-selected clusters, the observed color distribution of YGR clusters makes it highly likely that they do really have very low $q_{\rm PAH}$ fractions.

These characteristics are what we would expect from clusters that are located within H II regions rather than in the diffuse ISM, and confirm that YGR clusters identified with the HST F555W filter have already begun forming H II regions surrounded by PDRs even when the clusters are unresolved and their gas and dust morphology is smaller than a 4 pixel aperture. Based on these observations, even the youngest YGR clusters we observe in the PHANGS-HST catalog with the highest Hα EW are unlikely to have intracluster dust.

Individual clusters eliminate dust from their immediate vicinity quickly through feedback effects on the dust; the bulk of dust can be pushed outside our aperture sizes in as little as 2 Myr and at most 5 Myr (B. C. Whitmore et al. 2025). As clusters age and the most-massive stars start to evolve, supernovae and evolved stars become sources of non-natal dust within clusters and in the ISM after ∼5 Myr. Carbon-rich AGB stars are widely considered to be sites of PAH formation (W. B. Latter 1991), but have only been observed to have PAH spectral features when a hot massive companion star is present (C. Boersma et al. 2006). This is theorized to be because PAHs forming around AGB stars are shielded from UV radiation by the high optical opacity of carbonaceous dust. S-type AGB stars, on the other hand, have been observed to display PAH features at mid-IR wavelengths, likely due to lower opacity (K. Smolders et al. 2010). Analysis of the PAH ratios in H II regions indicates that areas with harder radiation fields exhibit a higher proportion of small PAHs (J. Chastenet et al. 2023). Since we do not observe clusters of any age to have a measurable 3.3 μm feature except when they also exhibit Hα emission, while evolved stars are likely the site of new PAH formation, they do not appear to create a measurable 3.3 μm PAH feature in our cluster catalog. This may be because we lack the sensitivity to detect the fresh PAHs from AGB stars,

or may be because the PAHs produced by AGB stars do not emit at 3.3 μm.

Since PAH fractions are observed to be lower in H II regions, and 3.3 μm-emitting small PAHs are observed to be less abundant in star-forming regions than in the diffuse ISM, YGR clusters that have already created H II regions require low $q_{\rm PAH}$ values for most accurate modeling of the 3.3 μm feature. The DL2014 dust models were developed for large patches of the ISM (B. T. Draine et al. 2014, M. Chevance et al. 2020) without incorporating sources (e.g., dust formation) or sinks (e.g., destruction through supernova blast waves), and thus, for a fixed dust grain population, any differences in dust emission are due to differences in radiation field or geometry effects. As a result, the models have a very coarse sampling at lower $q_{\rm PAH}$ values. Figure 20 illustrates the necessity of $q_{\rm PAH}$ values between 0.47 and 1.77 (the two lowest $q_{\rm PAH}$ values in DL2014).

Given literature that indicates that small PAHs are much less abundant compared to large PAHs in H II regions and dense PDRs than they are in the more diffuse ISM, the use of a dust model that does not include grain destruction is inherently limited on small scales. On the scale of star clusters, dust models must incorporate the rapid destruction of small PAHs, especially if incorporating both small and large PAH features in modeling. This changing ratio can provide valuable information about unresolved YGR clusters' formation of H II regions, which in turn will inform our ability to accurately age-date them.

5.3. Energy Balance with Small Apertures

CIGALE operates on the assumption that all starlight energy lost through attenuation is reprocessed in equal amounts as dust emission (energy balance). If observations of the local dust population being heated by a stellar cluster is fully contained within the aperture, this assumption by CIGALE is accurate (Cluster (a) in Figure 19 is an example of such a cluster). But once an H II region/PDR has expanded beyond our aperture, the assumption of energy balance within the aperture becomes less valid.

When dust emission extends beyond the photometric aperture (as is the case for the majority of YGR clusters), the inferred dust attenuation will be biased to slightly lower values, and in turn, the stellar ages are biased in favor of slightly older (6–10 Myr) solutions. Although other features of YGR clusters' SEDs work to counteract this effect (namely, strong Hα, which is linked to young age in the nebular emission model), it should not be discounted. Because of this effect, when we perform SED fitting with HST and NIRCam filters but without including Hα observations, our YGR clusters' modeled ages shift slightly older overall than would be expected given all of their other traits. This effect especially influences the modeled ages of clusters with both strong Hα and significant dust, and is much less pronounced in YGR clusters whose NIR SEDs are mostly or entirely stellar continuum.

Because DL2014 does not include dust sources and sinks, and since CIGALE/DL2014 does not factor geometry or expansion beyond the observed region, SED modeling with dust emission poses a challenge to fitting the number of clusters in the PHANGS-HST/JWST cluster catalog. With several thousand star clusters currently and more still to come, individually choosing apertures that incorporate all dust emission is prohibitively time consuming. Given the morphological complexity of star-forming regions that we see, even modeling each cluster with a custom aperture faces major challenges in determining the sources of observed dust emission. For these reasons, a small-aperture approach that incorporates how evolution over time affects dust energy balance would be most likely to be feasible to apply on the scale of our catalog. This approach is also most likely to accommodate the effects of differing resolutions: PHANGS-JWST also includes MIRI data of all galaxies, which has much lower resolution than HST and NIRCam.

6. Summary

This work presents an analysis of the impacts of incorporating high-resolution Hα narrowband and JWST NIRCam data, in addition to HST NUV-optical broadband data into SED fitting of star clusters in nearby galaxies. We especially investigate NIRCam's ability to break age–reddening degeneracies.

When we combine HST broadband and Hα narrowband with JWST NIRCam data, and use observational markers of optical color and Hα strength to constrain modeling priors, we find the following:

1. An EW(Hα) = 80 Å is accurate at identifying young (<10 Myr) gas-rich clusters. Clusters with EW just above this threshold are appropriately modeled with $f_{\rm esc}$ of 0.8–1, which provides continuity with exposed young clusters with lower Hα EW values. There is minimal contamination of completely exposed or older clusters, with 4/151 or 2.6% of clusters with EW(Hα) = 80 Å, which were individually evaluated being deemed to be >10 Myr or fitted poorly with the YGR grid.
2. The distribution of cluster ages in the first 10 Myr is relatively even, and does not exhibit the overdensity of 1 Myr clusters found when SED fitting with NUV-optical broadband filters only.
3. The addition of NIRCam allows us to accurately model clusters that are prone to a degeneracy between young and intermediate ages. It especially helps constrain the reddening of young clusters, and demonstrates that NUV-optical broadband modeling predicts unrealistically large reddening for many young clusters.
4. Improved constraints on dust abundance provided by NIR observations of hot dust demonstrate that BC03 stellar synthesis models in the first 10 Myr do not align with the distribution of a large sample of actual young clusters.
5. NIRCam and Hα do not significantly improve our ability to identify OGCs via four-filter color space, but may enable improved identification when combining all 10 NUV-optical-NIR filters.
6. A very low $q_{\rm PAH}$ mass fraction aligns best with the strength of the 3.3 μm PAH feature for all HST-identified YGR clusters, even for the youngest and most morphologically concentrated clusters. The high number of young, gas- and dust-rich clusters with strong, concentrated Hα, and rings or partial shells of 3.3 μm emission outside the cluster aperture, indicates the need for dynamical factors such as grain destruction and stellar

winds when incorporating the 2–3.6 μm range into SED fitting of young, gas-rich clusters.

An additional 16 PHANGS-HST galaxies are being imaged with narrowband Hα in HST Cycle 31, and 55 PHANGS-HST galaxies have been observed in JWST Cycle 2, bringing the total number of galaxies with HST broadband, Hα, and JWST observations to 74. We plan to expand our SED modeling to this larger sample as data become available, as well as robustly test the accuracy of an expanded set of stellar models to determine which, if any, align well with actual observations of star clusters.

Acknowledgments

This work is based on observations made with the NASA/ESA/CSA JWST and Hubble Space Telescopes. The data were obtained from the Mikulski Archive for Space Telescopes at the Space Telescope Science Institute, which is operated by the Association of Universities for Research in Astronomy, Inc., under NASA contract NAS 5-03127 for JWST and NASA contract NAS 5-26555 for HST. The JWST observations are associated with Program 2107, and those from HST with Programs 15454 and 17126.

This work has been supported by the French government, through the UCA^{JEDI} Investments in the Future project managed by the National Research Agency (ANR) with the reference number ANR-15-IDEX-01.

M.B. acknowledges support from FONDECYT regular grant 1211000 and by the ANID BASAL project FB210003. This work was supported by the French government through the France 2030 investment plan managed by the National Research Agency (ANR), as part of the Initiative of Excellence of Université Côte d'Azur under reference No. ANR-15-IDEX-01. F.P. acknowledges support from the Horizon Europe research and innovation program under the Marie Skłodowska-Curie grant "TraNSLate" No. 101108180, and from the Agencia Estatal de Investigación del Ministerio de Ciencia e Innovación (MCIN/AEI/ 10.13039/501100011033) under grant (PID2021-128131NB-I00) and the European Regional Development Fund (ERDF) "A way of making Europe." A.W. acknowledges UNAM's DGAPA for the support in carrying out her sabbatical stay at UCSD, USA, through program PASPA.

ORCID iDs

Kiana F. Henny https://orcid.org/0000-0001-7448-1749
Daniel A. Dale https://orcid.org/0000-0002-5782-9093
Rupali Chandar https://orcid.org/0000-0003-0085-4623
Médéric Boquien https://orcid.org/0000-0003-0946-6176
David A. Thilker https://orcid.org/0000-0002-8528-7340
Bradley C. Whitmore https://orcid.org/0000-0002-3784-7032
Janice C. Lee https://orcid.org/0000-0002-2278-9407
M. Jimena Rodriguez https://orcid.org/0000-0002-0579-6613
Daniel Maschmann https://orcid.org/0000-0001-6038-9511
Aida Wofford https://orcid.org/0000-0001-8289-3428
Rémy Indebetouw https://orcid.org/0000-0002-4663-6827
Leonardo Úbeda https://orcid.org/0000-0001-7130-2880
Brent Groves https://orcid.org/0000-0002-9768-0246
Hamid Hassani https://orcid.org/0000-0002-8806-6308
Kirsten L. Larson https://orcid.org/0000-0003-3917-6460
Thomas G. Williams https://orcid.org/0000-0002-0012-2142
Kathryn Grasha https://orcid.org/0000-0002-3247-5321
Francesca Pinna https://orcid.org/0000-0001-5965-3530
Stephen Hannon https://orcid.org/0000-0001-9628-8958

References

Adamo, A., Ryon, J. E., Messa, M., et al. 2017, ApJ, 841, 131
Anand, G. S., Lee, J. C., Van Dyk, S. D., et al. 2021, MNRAS, 501, 3621
Anders, P., & Fritze-v. Alvensleben, U. 2003, A&A, 401, 1063
Andrews, J. E., Calzetti, D., Chandar, R., et al. 2014, ApJ, 793, 4
Ashworth, G., Fumagalli, M., Krumholz, M. R., et al. 2017, MNRAS, 469, 2464
Barnes, A. T., Chandar, R., Kreckel, K., et al. 2022, A&A, 662, L6
Barnes, A. T., Glover, S. C. O., Kreckel, K., et al. 2021, MNRAS, 508, 5362
Baron, D., Sandstrom, K. M., Rosolowsky, E., et al. 2024, ApJ, 968, 24
Belfiore, F., Santoro, F., Groves, B., et al. 2022, A&A, 659, A26
Bialopetravičius, J., & Narbutis, D. 2020, A&A, 633, A148
Bialopetravičius, J., Narbutis, D., & Vansevičius, V. 2019, A&A, 621, A103
Boersma, C., Hony, S., & Tielens, A. G. G. M. 2006, A&A, 447, 213
Boquien, M., Burgarella, D., Roehlly, Y., et al. 2019, A&A, 622, A103
Boquien, M., Bendo, G., Calzetti, D., et al. 2010, ApJ, 713, 626
Bruzual, G., & Charlot, S. 2003, MNRAS, 344, 1000
Calzetti, D., Lee, J. C., Sabbi, E., et al. 2015, AJ, 149, 51
Cardelli, J. A., Clayton, G. C., & Mathis, J. S. 1989, ApJ, 345, 245
Catinella, B., Saintonge, A., Janowiecki, S., et al. 2018, MNRAS, 476, 875
Cesarsky, D., Lequeux, J., Abergel, A., et al. 1996, A&A, 315, L309
Chabrier, G. 2003, PASP, 115, 763
Chastenet, J., Sandstrom, K., Chiang, I.-D., et al. 2019, ApJ, 876, 62
Chastenet, J., Sutter, J., Sandstrom, K., et al. 2023, ApJL, 944, L11
Chevance, M., Kruijssen, J. M. D., Hygate, A. P. S., et al. 2020, MNRAS, 493, 2872
Chown, R., Sidhu, A., Peeters, E., et al. 2024, A&A, 685, A75
Cook, D. O., Lee, J. C., Adamo, A., et al. 2019, MNRAS, 484, 4897
Cook, D. O., Lee, J. C., Adamo, A., et al. 2023, MNRAS, 519, 3749
Dale, D. A., Boquien, M., Barnes, A. T., et al. 2023, ApJL, 944, L23
Dale, D. A., Helou, G., Magdis, G. E., et al. 2014, ApJ, 784, 83
Davies, B., Figer, D. F., Kudritzki, R.-P., et al. 2007, ApJ, 671, 781
Deger, S., Lee, J. C., Whitmore, B. C., et al. 2022, MNRAS, 510, 32
Deshmukh, S., Linden, S. T., Calzetti, D., et al. 2024, ApJL, 974, L24
Dolphin, A., 2016 DOLPHOT: Stellar Photometry, Astrophysics Source Code Library, ascl:1608.013
Draine, B. T., Aniano, G., Krause, O., et al. 2014, ApJ, 780, 172
Draine, B. T., Dale, D. A., Bendo, G., et al. 2007, ApJ, 663, 866
Egorov, O. V., Kreckel, K., Sandstrom, K. M., et al. 2023, ApJL, 944, L16
Emsellem, E., Schinnerer, E., Santoro, F., et al. 2022, A&A, 659, A191
Fan, Z., Li, Z., & Zhao, G. 2018, AJ, 156, 191
Ferland, G. J. 1980, PASP, 92, 596
Floyd, M., Chandar, R., Whitmore, B. C., et al. 2024, AJ, 167, 95
Fouesneau, M., & Lançon, A. 2010, A&A, 521, A22
Fouesneau, M., Lançon, A., Chandar, R., & Whitmore, B. C. 2012, ApJ, 750, 60
Goudfrooij, P., Puzia, T. H., Kozhurina-Platais, V., & Chandar, R. 2011, ApJ, 737, 3
Grasha, K., Calzetti, D., Adamo, A., et al. 2015, ApJ, 815, 93
Gregg, B., Calzetti, D., Adamo, A., et al. 2024, ApJ, 971, 115
Groves, B., Dopita, M. A., Sutherland, R. S., et al. 2008, ApJS, 176, 438
Groves, B., Kreckel, K., Santoro, F., et al. 2023, MNRAS, 520, 4902
Hannon, S., Lee, J. C., Whitmore, B. C., et al. 2019, MNRAS, 490, 4648
Hannon, S., Lee, J. C., Whitmore, B. C., et al. 2022, MNRAS, 512, 1294
Hannon, S., Whitmore, B. C., Lee, J. C., et al. 2023, MNRAS, 526, 2991
Harris, W. E. 2010, arXiv:1012.3224
Inoue, A. K. 2011, MNRAS, 415, 2920
Johnson, L. C., Seth, A. C., Dalcanton, J. J., et al. 2012, ApJ, 752, 95
Johnson, L. C., Wainer, T. M., Torresvillanueva, E. E., et al. 2022, ApJ, 938, 81
Kim, H., Whitmore, B. C., Chandar, R., et al. 2012, ApJ, 753, 26
Kreckel, K., Ho, I. T., Blanc, G. A., et al. 2019, ApJ, 887, 80
Krumholz, M. R., Fumagalli, M., da Silva, R. L., Rendahl, T., & Parra, J. 2015, MNRAS, 452, 1447
Latter, W. B. 1991, ApJ, 377, 187
Lee, J. C., Sandstrom, K. M., Leroy, A. K., et al. 2023, ApJL, 944, L17
Lee, J. C., Whitmore, B. C., Thilker, D. A., et al. 2022, ApJS, 258, 10
Leroy, A. K., Schinnerer, E., Hughes, A., et al. 2021, ApJS, 257, 43

Maschmann, D., Lee, J. C., Thilker, D. A., et al. 2024a, ApJS, 273, 14
Maschmann, D., Lee, J. C., Thilker, D. A., et al. 2024b, ApJS, 273, 14
McQuaid, T., Calzetti, D., Linden, S. T., et al. 2024, ApJ, 967, 102
Messa, M., Adamo, A., Calzetti, D., et al. 2018a, MNRAS, 477, 1683
Messa, M., Adamo, A., Östlin, G., et al. 2018b, MNRAS, 473, 996
Mouhcine, M., & Lançon, A. 2002, A&A, 393, 149
Narloch, W., Pietrzyński, G., Gieren, W., et al. 2022, A&A, 666, A80
Nayak, P. K., Subramaniam, A., Choudhury, S., & Sagar, R. 2018, A&A, 616, A187
Oey, M. S., Meurer, G. R., Yelda, S., et al. 2007, ApJ, 661, 801
Orozco-Duarte, R., Wofford, A., Vidal-Garcìa, A., et al. 2022, MNRAS, 509, 522
Pedrini, A., Adamo, A., Calzetti, D., et al. 2024, ApJ, 971, 32
Pérez, G., Messa, M., Calzetti, D., et al. 2021, ApJ, 907, 100
Querejeta, M., Schinnerer, E., Meidt, S., et al. 2021, A&A, 656, A133
Rayner, J. T., Cushing, M. C., & Vacca, W. D. 2009, ApJS, 185, 289
Reines, A. E., Nidever, D. L., Whelan, D. G., & Johnson, K. E. 2010, ApJ, 708, 26
Rodriguez, J., Lee, J., Whitmore, B., et al. 2023, ApJL, 944, L26
Sabbi, E., Calzetti, D., Ubeda, L., et al. 2018, ApJS, 235, 23
Sacchi, E., Cignoni, M., Aloisi, A., et al. 2019, ApJ, 878, 1
Sandstrom, K. M., Bolatto, A. D., Bot, C., et al. 2012, ApJ, 744, 20
Sandstrom, K. M., Chastenet, J., Sutter, J., et al. 2023, ApJL, 944, L7
Smolders, K., Acke, B., Verhoelst, T., et al. 2010, A&A, 514, L1
Sutter, J., Sandstrom, K., Chastenet, J., et al. 2024, ApJ, 971, 178
Tang, J., Grasha, K., & Krumholz, M. R. 2024, MNRAS, 532, 4583
Theulé, P., Burgarella, D., Buat, V., et al. 2024, A&A, 682, A119
Thilker, D. A., Lee, J. C., Whitmore, B. C., et al. 2025, ApJS, 280, 1
Thilker, D. A., Whitmore, B. C., Lee, J. C., et al. 2022, MNRAS, 509, 4094
Turner, J. A., Dale, D. A., Lee, J. C., et al. 2021, MNRAS, 502, 1366
Wei, W., Huerta, E. A., Whitmore, B. C., et al. 2020, MNRAS, 493, 3178
Weidner, C., Kroupa, P., & Larsen, S. S. 2004, MNRAS, 350, 1503
Weisz, D. R., Dolphin, A. E., Skillman, E. D., et al. 2013, MNRAS, 431, 364
Whitmore, B. C., Chandar, R., Kim, H., et al. 2011, ApJ, 729, 78
Whitmore, B. C., Chandar, R., Lee, J., et al. 2020, ApJ, 889, 154
Whitmore, B. C., Chandar, R., Lee, J. C., et al. 2023, MNRAS, 520, 63
Whitmore, B. C., Chandar, R., Lee, J. C., et al. 2025, ApJ, 982, 50
Whitmore, B. C., Lee, J. C., Chandar, R., et al. 2021, MNRAS, 506, 5294
Williams, B. F., Dalcanton, J. J., Bell, E. F., et al. 2012, ApJ, 759, 46
Williams, T. G., Lee, J. C., Larson, K. L., et al. 2024, ApJS, 273, 13
Wofford, A., Leitherer, C., & Chandar, R. 2011, ApJ, 727, 100